

## Dopamine Activates Astrocytes in Prefrontal Cortex via $\alpha 1$ -Adrenergic Receptors

Silvia Pittolo<sup>1,2</sup>, Sae Yokoyama<sup>1</sup>, Drew D. Willoughby<sup>1,3</sup>, Charlotte R. Taylor<sup>1,3</sup>, Michael E. Reitman<sup>1,3</sup>, Vincent Tse<sup>1</sup>, Zhaofa Wu<sup>4</sup>, Roberto Etchenique<sup>5</sup>, Yulong Li<sup>4</sup>, Kira E. Poskanzer<sup>1,3,6\*</sup>

<sup>1</sup> Department of Biochemistry & Biophysics, University of California, San Francisco, San Francisco, CA, USA

<sup>2</sup> Current address: Max Delbrück Center for Molecular Medicine in the Helmholtz Association, Robert-Rössle-Str. 10, 13125 Berlin, Germany

<sup>3</sup> Neuroscience Graduate Program, University of California, San Francisco, San Francisco, CA, USA

<sup>4</sup> State Key Laboratory of Membrane Biology, Peking University School of Life Sciences, Beijing 100871, China; Peking-Tsinghua Center for Life Sciences, Peking University, Beijing 100871, China

<sup>5</sup> Departamento de Química Inorgánica, Analítica y Química Física, INQUIMAE, Facultad de Ciencias Exactas y Naturales, Universidad de Buenos Aires, CONICET, Intendente Güiraldes 2160, Ciudad Universitaria, Pabellón 2, Buenos Aires (C1428EGA), Argentina

<sup>6</sup> Kavli Institute for Fundamental Neuroscience, San Francisco, CA, USA

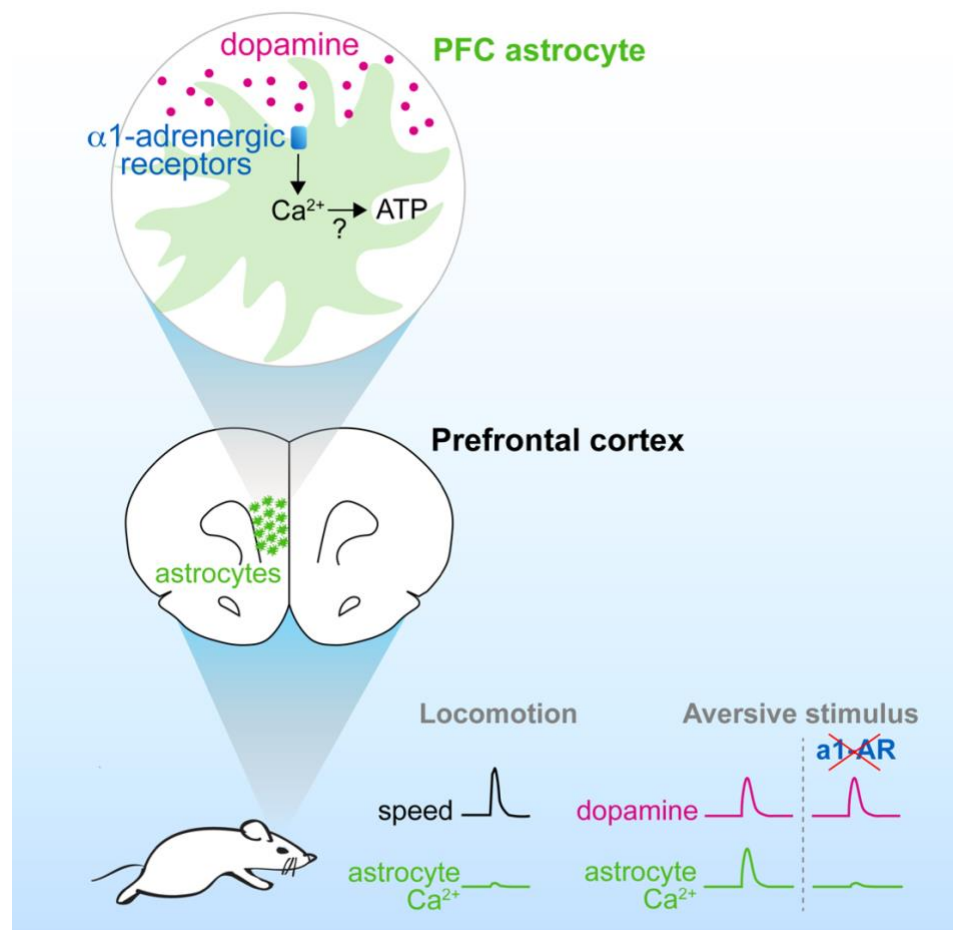
\***Lead contact:** Kira Poskanzer ([kira.poskanzer@ucsf.edu](mailto:kira.poskanzer@ucsf.edu))

**Keywords:** Prefrontal cortex, astrocytes, dopamine, adrenergic receptors, calcium, two-photon imaging, fiber photometry, cAMP, aversive stimulus, ATP, receptor interactions, GPCR signaling

## Summary

The prefrontal cortex (PFC) is a hub for cognitive control, and dopamine profoundly influences its functions. In other brain regions, astrocytes sense diverse neurotransmitters and neuromodulators and, in turn, orchestrate regulation of neuroactive substances. However, basic physiology of PFC astrocytes, including which neuromodulatory signals they respond to and how they contribute to PFC function, is lacking. Here, we characterize divergent signaling signatures in astrocytes of PFC and primary sensory cortex in mice, which are linked to differential responsivity to locomotion. We find that PFC astrocytes express receptors for dopamine, but are unresponsive through the  $G_s/G_i$ -cAMP pathway. Instead, fast calcium signals in PFC astrocytes are time-locked to dopamine release, and are mediated by  $\alpha 1$ -adrenergic receptors both *ex vivo* and *in vivo*. Further, we describe dopamine-triggered regulation of extracellular ATP at PFC astrocyte territories. Thus, we identify astrocytes as active players in dopaminergic signaling in PFC, contributing to PFC function through neuromodulator receptor crosstalk.

## Graphical Abstract



## Introduction

The prefrontal cortex (PFC) is a higher order association cortex that integrates and holds sensory and cognitive information from other brain areas to organize and execute behavior (Fuster et al., 2000). The PFC is involved in fundamental and diverse processes, including working memory and attention (Funahashi et al., 1989; Fuster and Alexander, 1971; Kesner et al., 1996), behavioral flexibility and planning (Dias et al., 1996; Ragozzino et al., 1999), and sustained processing of stress, fear and emotions (George et al., 1995; Hariri et al., 2003; Kim et al., 2003; Milad and Quirk, 2002). Despite its importance, how the PFC performs many aspects of its complex functions is still poorly understood. For instance, whether persistent activity of individual PFC neurons or rather network dynamics underlie the ability of the PFC to hold information over multi-second delays during working memory tasks is subject of current debate (Barbosa et al., 2020; Cavanagh et al., 2018; Constantinidis et al., 2018; Inagaki et al., 2019; Park et al., 2019; Spaak et al., 2017).

While prefrontal circuits are fundamental for the top-down control of behavior, ascending arousal systems—including the mesocortical dopamine (DA) pathway—are so necessary for PFC executive functions that their disruption recapitulates PFC lesions (Brozoski et al., 1979). Dopaminergic projections to the PFC are particularly sensitive to stressful and aversive stimuli (Abercrombie et al., 1989; Lammel et al., 2012; Thierry et al., 1976; Vander Weele et al., 2018). However, how both fast (phasic) and prolonged (tonic) temporal patterns of DA release play specific roles in PFC computations is unclear (Lohani et al., 2019), with evidence for bidirectional or opposing effects on the excitability of prefrontal neuron subtypes (Anastasiades et al., 2019; Chen et al., 2007; Gao and Goldman-Rakic, 2003; Gao et al., 2003; Huang et al., 2004; Kröner et al., 2007; Matsuda et al., 2006; Seamans et al., 2001; Vijayraghavan et al., 2007) which ultimately contribute to the complex patterns of sustained and dynamic circuit activity underlying PFC functions.

Astrocytes—the most abundant non-neuronal brain cell type—are also well positioned to receive and process neuronal signals, as they are equipped with an array of receptors for neurotransmitters and neuromodulators (Porter and McCarthy, 1997) and have wide, non-overlapping territories, each encompassing thousands of synapses (Bushong et al., 2002). Many lines of research show that astrocytes are in a bidirectional dialogue with neurons, by sensing neuronal activity through G protein-coupled receptors (GPCRs) (Kofuji and Araque, 2021), internally computing through  $\text{Ca}^{2+}$  and cAMP signals (Oe et al., 2020; Srinivasan et al., 2016), and regulating neuroactive substances such as glutamate (Bezzi et al., 2004; Yang et al., 2019) and ATP (Cao et al., 2013; Pascual et al., 2005; Zhang et al., 2003) that can influence local synaptic plasticity and network connectivity on multiple spatiotemporal scales (Pاناتier et al., 2011; Perea and Araque, 2007; Poskanzer and Yuste, 2016). Previous work shows that chemical ablation of PFC astrocytes, blockade of glutamate/glutamine homeostasis or DA uptake and metabolism,

impaired gliotransmission,  $\text{Ca}^{2+}$  or ATP signals, or lack of  $\text{GABA}_B$  receptors in PFC astrocytes cause depressive (Banasr and Duman, 2008; Cao et al., 2013; John et al., 2012; Lee et al., 2013) or autism-like behaviors (Wang et al., 2021), and interfere with working memory (Lima et al., 2014; Mederos et al., 2021; Petrelli et al., 2020; Sardinha et al., 2017). With these notable exceptions, decades of research have largely neglected the contribution of astrocyte physiology to PFC regulation.

Here, we use a combination of *in vivo* two-photon (2P) imaging, fiber photometry, and *ex vivo* imaging of calcium ( $\text{Ca}^{2+}$ ), cAMP, neuromodulators, and ATP to explore astrocyte signals in PFC. We first characterize endogenous  $\text{Ca}^{2+}$  dynamics of PFC astrocytes *in vivo* through GRIN lens imaging (Levene et al., 2004), and compare them to primary sensory cortical astrocytes. We find that PFC astrocytes display unique spatiotemporal signals compared to those in primary visual cortex (V1), and lack responsiveness to locomotory activity observed in sensory cortex (Paukert et al., 2014; Wang et al., 2019). We next demonstrate that PFC astrocytes express dopamine receptors (DR), but signal through fast, sustained  $\text{Ca}^{2+}$  mobilizations rather than the canonical  $\text{G}_s/\text{G}_i$ -cAMP pathway. Unexpectedly, we find that DA in PFC elicits astrocyte activation through the  $\text{G}_q$ -coupled  $\alpha 1$ -AR, which we confirmed by pharmacological screening with DR and adrenergic receptor (AR) inhibitors both in acute slices and *in vivo*. Finally, we show that PFC astrocytes can regulate extracellular ATP in response to DA, which may contribute to neuronal computation in PFC. Together, our data demonstrate that astrocytes in PFC sense neuromodulators and behavioral stimuli differently than sensory cortical astrocytes. By exploring the physiology of PFC astrocytes, we uncover functional crosstalk—both *ex vivo* and *in vivo*—between DA and receptors for norepinephrine (NE).

## Results

### *PFC astrocytes exhibit more single-cell restricted $\text{Ca}^{2+}$ activity compared to sensory cortex*

Since PFC is an associative cortical area (Fuster et al., 2000), we hypothesized that astrocyte  $\text{Ca}^{2+}$  in PFC may have unique properties compared to primary sensory cortices, where population-level bursts of activity have been well documented (Bekar et al., 2008; Ding et al., 2013; Slezak et al., 2019; Srinivasan et al., 2016; Wang et al., 2019). To test this, we compared spontaneous astrocyte  $\text{Ca}^{2+}$  activity in PFC and primary visual cortex (V1) using two-photon (2P) microscopy in head-fixed mice. To gain imaging access, we implanted either a GRIN lens (Levene et al., 2004) over PFC or a cranial window over V1 in mice expressing Lck-GCaMP6f (Fig 1A) (Shigetomi et al., 2010; Srinivasan et al., 2016) under the astrocyte-specific promoter *GfaABC1D*. GRIN lens positioning was confirmed post-mortem (Fig S1A), and GFAP staining was used to assess low astrocyte reactivity around the implant (Fig S1B).

Using event-based image analyses to detect the area of astrocyte  $\text{Ca}^{2+}$  independent of pre-determined regions-of-interest (Wang et al., 2019), we observed that the largest astrocyte  $\text{Ca}^{2+}$  signals in PFC often

appeared to be the size of a single astrocyte ( $\sim 50 \times 50 \mu\text{m}$ ; Fig 1B–C top), whereas the population-level, burst-like events in V1 span the entire imaging field (here:  $300 \times 300 \mu\text{m}$ ; Fig 1B–C bottom), as previously reported (Slezak et al., 2019; Srinivasan et al., 2016; Wang et al., 2019). We thus focused on these larger events ( $>1000 \mu\text{m}^2$ ) for quantitative comparison (Fig 1D–H), and found that while astrocyte  $\text{Ca}^{2+}$  events occur at the same rate in PFC and V1 (Fig 1D), they are smaller (Fig 1E) and last longer (Fig 1F) in PFC. When examining the network properties of astrocyte  $\text{Ca}^{2+}$ , we found that events in PFC are less synchronous with other PFC events (Fig 1G), but tend to repeat more at the same locations in the imaging field compared to those in V1 (Fig 1H). Although less obvious by eye, smaller  $\text{Ca}^{2+}$  events ( $<1000 \mu\text{m}^2$ ) also differ between PFC and V1 (Fig S1C–G), indicating that overall  $\text{Ca}^{2+}$  dynamics may be driven by different mechanisms depending on brain region. Together, these data demonstrate that astrocyte  $\text{Ca}^{2+}$  dynamics in PFC are significantly different from those in V1, suggesting that astrocytes in PFC may play different functional roles than in primary sensory cortex.

#### *Population-level astrocyte $\text{Ca}^{2+}$ activity in PFC is not tightly linked to locomotion*

Since burst-like astrocyte activity in V1 is known to be driven by locomotion (Paukert et al., 2014; Slezak et al., 2019; Wang et al., 2019), we next wondered whether the observed differences in astrocyte  $\text{Ca}^{2+}$  dynamics in PFC compared to V1 were due to differences in astrocytic response to locomotion (Movie 1). To examine this, we aligned population-level astrocyte  $\text{Ca}^{2+}$  traces to the onset of locomotion bouts (Fig 1J–K and Fig S1H–I). Similar to previous results (Paukert et al., 2014; Slezak et al., 2019), average astrocyte  $\text{Ca}^{2+}$  in V1 significantly increases soon after locomotion onset (2.2 s), peaks at 6.2 s, and stays above baseline for the remaining 15 s (Fig 1K left, green). When we plot the distribution of the times at which we detect the maximum change in astrocyte  $\text{Ca}^{2+}$  (Fig 1K, right), we observe a clear peak 6–9 s after locomotion onset. In contrast, in PFC astrocytes we did not find significant and sustained  $\text{Ca}^{2+}$  increases at the onset of locomotion on average, and no clear peak for maximum change across trials is evident (Fig 1K, red). These results indicate that whereas V1 astrocytes are recruited soon after an animal begins locomotion, PFC astrocytes are not activated by locomotion on average, although we do not exclude the possibility that a few astrocytes or astrocytic domains are locomotion-linked.

These results suggest that astrocytic  $\text{Ca}^{2+}$  is not linked to locomotion in PFC. We next wondered whether  $\text{Ca}^{2+}$  events in PFC astrocytes are instead involved in the generation of locomotion. To explore this, we aligned locomotion traces to the onset of astrocyte  $\text{Ca}^{2+}$  events (Fig 1L–M, Fig S1J–K), and found no times around  $\text{Ca}^{2+}$  onsets when animal speed significantly deviated from average (Fig 1M left, red). When mice did move, the maximum speed was equally distributed over the time window around astrocyte  $\text{Ca}^{2+}$  (Fig 1M, right), suggesting that astrocytic  $\text{Ca}^{2+}$  activity in PFC is unlinked from locomotion. In contrast to PFC, astrocyte  $\text{Ca}^{2+}$ -aligned locomotion analysis in V1 shows that speed

increases starting at -5.1 s before  $\text{Ca}^{2+}$  event onset and until 2.2 s after, and peaks -1.1 s before  $\text{Ca}^{2+}$  onset (Fig 1M left, green), which is in accordance with previous observations that locomotion initiates  $\text{Ca}^{2+}$  activity in V1 astrocytes (Paukert et al., 2014; Slezak et al., 2019) (Fig 1J–K). Together, these results indicate that astrocyte activity in PFC differs significantly from that observed in V1, both in terms of  $\text{Ca}^{2+}$  event dynamics and their relationship with locomotion.

### *PFC astrocytes express dopamine receptors*

Because it has been previously shown that burst-like astrocyte population dynamics are mediated by noradrenergic signaling (Bekar et al., 2008; Ding et al., 2013; Paukert et al., 2014) and PFC astrocytes do not display this bursting activity (Fig 1B–C), we wondered whether another neuromodulator may be involved in the astrocyte activity we observe in PFC *in vivo*. We reasoned that since dopamine (DA) is an important neuromodulatory input for PFC neurons (Brozoski et al., 1979; Thierry et al., 1976), DA may also activate PFC astrocytes. To explore this possibility, we first examined DA receptor expression in prefrontal astrocytes by crossing the transgenic reporter lines *Drd1a*-tdTomato (Shuen et al., 2008) or *Drd2*-EGFP (Gong et al., 2003), which have been widely used to identify expression of D1R or D2R in neurons, to the astrocyte-specific reporter lines *Aldh11l1*-EGFP (Tsai et al., 2012) or *Aldh11l1*-tdTomato (Gong et al., 2003) (Fig 2A). We immunostained for the fluorophores in young adult mice (P29–32) and determined colocalization of these reporters in cell somata across PFC layers (Fig 2C–D and Fig S2A). We found that  $13 \pm 1\%$  of all *Aldh11l1*<sup>+</sup> cells colocalize with D1R and  $14 \pm 1\%$  colocalize with D2R (Fig 2C). Conversely,  $18 \pm 2\%$  of all D1R<sup>+</sup> cells, and  $41 \pm 3\%$  of all D2R<sup>+</sup> cells are *Aldh11l1*<sup>+</sup> (Fig 2D). For both receptors, colocalization with *Aldh11l1* in astrocytes was maximal in layer 1, consistent with the prevalence of neuronal projections rather than neuronal somata in the most superficial cortical layer. These results demonstrate expression of both D1R and D2R in PFC astrocytes, suggesting that PFC astrocytes may respond specifically to DA, as has been demonstrated in other brain regions (Chai et al., 2017; Corkrum et al., 2020; Cui et al., 2016; Fischer et al., 2020; Jennings et al., 2017; Xin et al., 2019).

### *Direct DA receptor stimulation does not recruit the canonical cAMP intracellular signaling pathway*

D1R and D2R are canonically coupled to  $G_s$ - and  $G_i$ -GPCR proteins, respectively. To test whether these receptors in PFC astrocytes lead to changes in intracellular cAMP when activated, we expressed the fluorescent cAMP reporter Pink Flamindo (Harada et al., 2017) in PFC astrocytes and performed *ex vivo* acute slice experiments from young adult mice (Fig 2E), while pharmacologically targeting DA receptors (Fig 2F–G). We blocked possible contributions from neighboring D1R<sup>+</sup> and D2R<sup>+</sup> neurons by inhibiting action potentials with TTX and preventing neuron-to-astrocyte communication with a multi-drug cocktail (see Methods). We first bath-applied 10  $\mu\text{M}$  DA (Fig 2F left, top; doses in these experiments were chosen

to reflect physiological levels of DA reported in the literature), and did not observe significant changes in average Pink Flamindo fluorescence (Fig 2G). However, because D1R and D2R have opposing effects on adenylate cyclase (AC), DA could in principle both stimulate and inhibit cAMP production. Thus, we searched at the single-cell level for both increases and decreases in Pink Flamindo fluorescence, and still did not observe changes after addition of DA (Fig S2B).

To expand on this unexpected negative result and distinguish between possible contributions of  $G_s$  and  $G_i$  signaling, we next directly activated either D1R or D2R with receptor subtype-specific agonists (D1: SKF81297, 10  $\mu$ M; D2: Quinpirole, 10  $\mu$ M) and imaged cAMP (Fig 2F left, middle–bottom). Again, we found no change from baseline in average cAMP levels for any of the drugs tested (Fig 2G). (Quinpirole is a full agonist at all D2-like dopamine receptors (D2, D3 and D4). However, because all D2-like receptors are coupled to  $G_s$  proteins—thus canonically linked to increases in cAMP levels—we assumed that this widely used D2 agonist would cause similar changes in cAMP regardless of the receptor subtype involved. Because no response to Quinpirole was detected, we did not explore this further.) To confirm that Pink Flamindo could detect changes in cAMP in our experiments, we followed each drug-treatment experiment with bath-application of the AC agonist Forskolin (10  $\mu$ M, Fig 2F right). Forskolin application led to a consistent increase in Pink Flamindo fluorescence relative to both baseline and drug treatment (Fig 2G and Fig S2B), which was comparable to Forskolin stimulation in naïve slices (in the absence of TTX and drug cocktail; Fig S2C). We confirmed that these results were not due to slice-to-slice variability (within-treatment comparisons, not significant; Fig 2G) or cell-to-cell differences in Pink Flamindo expression (Fig S2D), indicating that neither DA nor DR subtype-specific agonists induce detectable changes downstream of  $G_s$  or  $G_i$  effector proteins in PFC astrocytes.

#### *DA activates PFC astrocyte $Ca^{2+}$ signals via cell-surface adrenergic receptors*

While DRs on PFC may not recruit the cAMP pathway in our experimental conditions, previous research demonstrates 1) that DA can mobilize intracellular  $Ca^{2+}$  in astrocytes in hippocampus (Chai et al., 2017; Jennings et al., 2017), olfactory bulb (Fischer et al., 2020) and subcortical nuclei (Chai et al., 2017; Corkrum et al., 2020; Cui et al., 2016; Xin et al., 2019) and 2) DRs in neurons can activate non-canonical GPCR signaling pathways which result in  $Ca^{2+}$  mobilization (Lee et al., 2004; Medvedev et al., 2013; Sahu et al., 2009; Undie and Friedman, 1990). To test whether DA mobilizes intracellular  $Ca^{2+}$  in PFC astrocytes—and may be mediating the *in vivo*  $Ca^{2+}$  activity we described (Fig 1)—we expressed GCaMP6f in PFC astrocytes using viral vectors (Fig 3A–B), and carried out bath-application imaging experiments in acute slices, blocking neuronal activity with TTX and the drug cocktail as above. We found that bath-application of DA caused a large increase in astrocyte  $Ca^{2+}$  event frequency compared to baseline (Movie 2; Fig 3C–D, and Fig 3E pink). In contrast, application of D1 and D2 receptor agonists

(SKF38393 and Quinpirole, 10  $\mu$ M) had no discernible effect on  $\text{Ca}^{2+}$  activity (Fig 3E, yellow; Fig S3A top left). To test whether DRs are engaged in mediating the DA-dependent increase in intracellular  $\text{Ca}^{2+}$ , we next bath-applied DA in the presence of the DR antagonists SCH23390 and Sulpiride, and observed a partial inhibition of astrocyte  $\text{Ca}^{2+}$  dynamics (Fig S3A, top right), although no significant decrease in event rate compared to application of DA alone (Fig 3D, blue).

Since the effect of DA on PFC astrocyte  $\text{Ca}^{2+}$  is minimally inhibited by antagonists of DRs, we next tested whether the robust  $\text{Ca}^{2+}$  response to DA is mediated by GPCRs at all. To do so, we carried out DA-application and GCaMP imaging experiments in slices obtained from mice genetically lacking  $\text{IP}_3\text{R}2$  (Li et al., 2005), the main intracellular receptor downstream of GPCRs in astrocytes that mediates intracellular  $\text{Ca}^{2+}$  release (Pettravicz et al., 2008; Zhang et al., 2014). In these slices, we observed a significant inhibition of  $\text{Ca}^{2+}$  mobilization by DA (Fig 3D, gray and Fig S3A, bottom left), suggesting that PFC astrocytes do indeed rely on GPCR signaling to mediate the  $\text{Ca}^{2+}$  response to DA. Because DA has been shown to act on adrenergic receptors (ARs) in neurons (Alachkar et al., 2010; Cilz et al., 2014; Cornil et al., 2002; Guiard et al., 2008; Marek and Aghajanian, 1999; Özkan et al., 2017), we next carried out DA-application in the presence of broad-spectrum adrenergic receptor antagonists ( $\alpha 1/\alpha 2$ : Phentolamine;  $\beta$ : Propranolol; 10  $\mu$ M). In contrast to the effect of DRs antagonists, blocking ARs completely abolished the DA-mediated increase in  $\text{Ca}^{2+}$  activity (Fig 3C, green and Fig S3A, bottom right).

Because the astrocyte recruitment by bathed DA had an onset on the order of minutes and was sensitive to ARs inhibitors, we hypothesized that DA could be transformed to NE, a one-step enzymatic product of DA (Kirshner, 1957). To confirm that PFC astrocytes were indeed responding to DA and not NE, we imaged acute PFC slices in which the fluorescent sensor  $\text{GRAB}_{\text{NE}}$  was expressed throughout the tissue (Fig 3F), and bath-applied either DA or NE. In these experiments, DA did not induce a significant change in  $\text{GRAB}_{\text{NE}}$  fluorescence compared to the baseline period, in contrast to a large response to NE (Fig 3G), suggesting that the observed response to DA mediated by ARs (Fig 3C) is not linked to conversion of DA to NE *in situ*. Lastly, we wanted to test whether DA induced PFC astrocyte  $\text{Ca}^{2+}$  via GPCR signaling from the plasma membrane, or via intracellular compartments, since GPCR signaling can occur or be amplified on internal organelles (Calebiro et al., 2009; Irannejad et al., 2013; Kotowski et al., 2011) and dopaminergic antagonists can display low membrane-permeability (Dos Santos Pereira et al., 2014). To do this, we imaged PFC astrocyte  $\text{Ca}^{2+}$  (using the indicator Fluo-4) in organic cation transporter 3 knockout mice ( $\text{OCT}3^{-/-}$ , Fig 3H), in which the intracellular transport of monoamines including DA is blocked (Amphoux et al., 2006; Cui et al., 2009; Duan and Wang, 2010; Zwart et al., 2001). Bath-application of DA in slices from these animals (Fig 3I left) led to a robust increase in Fluo-4 fluorescence compared to baseline (Fig 3I right), suggesting that DA acts on cell-surface GPCRs in PFC astrocytes.

### *Physiological concentrations of DA evoke fast, transient Ca<sup>2+</sup> signals in PFC astrocytes*

The previous experiments demonstrated that PFC astrocytes respond to continuous application of DA with increases in intracellular Ca<sup>2+</sup>, although with a slow onset. We next explored whether astrocytes can also be engaged by acute stimuli that better reflect physiological dynamics of DA in the brain. To do so, we turned to one-photon (1P) photoactivation of a caged form of DA (RuBi-DA, Fig 4A–B) (Araya et al., 2013), which allowed us to achieve fast release and to mimic volume transmission (Agnati et al., 1995; Banerjee et al., 2020), the main modality of DA release in PFC. We first validated our light-stimulation protocol by comparing a DA dose-response curve (Fig 4C and Fig S4A) to photoactivation of RuBi-DA (Fig 4D and Fig S4B left) in PFC slices expressing the fluorescent DA sensor dLight (Patriarchi et al., 2018). We used these methods to estimate the concentration of DA across the imaging field, and found that our photoactivation protocol released on average ~2 μM DA (Fig 4E), which matches physiological levels of DA detected by voltammetry in PFC *in vivo* (Garris and Wightman, 1994) and DA concentration estimates near release sites in other brain areas (Courtney and Ford, 2014; Patriarchi et al., 2018).

Next, to understand how single PFC astrocytes respond to temporally controlled DA release, we uncaged RuBi-DA in slices with GCaMP-expressing astrocytes (Fig 4F top, Movie 3) while blocking neurons with TTX and drug cocktail as above. For analysis, we drew borders around each cell (Fig 4F, bottom) and detected Ca<sup>2+</sup> events using AQUA within these single-cell maps, which allowed us to map Ca<sup>2+</sup> event features within cells (Fig 4G–I) and monitor the amount of cell recruited over time (Fig 4J–L) in response to temporally precise DA release. In control conditions (no RuBi-DA; Fig 4G–H, left), the majority of astrocytes (91%) were inactive throughout the trial and similar numbers of cells increased or decreased their Ca<sup>2+</sup> event activity around the LED pulse (4%). In contrast, in presence of RuBi-DA (Fig 4G–H, right), the majority of astrocytes across all cortical layers responded to uncaging with an increase in activity (62%) rather than a decrease (4%). We next explored the Ca<sup>2+</sup> event features induced by uncaging in individual astrocytes, and found that events were more abundant, larger, and lasted longer following LED stimulation in RuBi-DA, but not in the controls (Fig 4I). We confirmed that these results were not affected by the pharmacological cocktail used since all features of Ca<sup>2+</sup> events were unchanged compared to naïve slices (Fig S4C–D).

When looking at the overall Ca<sup>2+</sup> mobilization within individual astrocytes (Fig 4K), we observed that Ca<sup>2+</sup> activity was induced with a short response time (8.6 s, Fig 4K, L, left) and short duration (9.9 s, Fig 4K, middle) in most cells, whereas the amount of cell recruited by fast DA release varied considerably between cells (49%, Fig 4K, right). We confirmed that the results we obtained were not affected by our single-cell delineation method, as we found no correlation between cell size and amount

of cell surface recruited by DA (Fig S4E). These data demonstrate that astrocytes respond acutely to physiological levels of extracellular DA with fast and transient  $\text{Ca}^{2+}$  dynamics that cover different astrocyte territories across cells.

#### *PFC astrocytes require $\alpha 1$ -AR signaling to respond to DA*

Our bath application experiments suggested that ARs—but not DRs—mediate signaling downstream of DA in PFC astrocytes (Fig 3E). To explore the contribution of DRs and ARs to fast dopaminergic stimulation of astrocytes, we photoreleased DA as described above on PFC slices treated with different subtype-specific inhibitors of DA and NE receptors (Fig 5A, Movie 4). We monitored population-level astrocyte  $\text{Ca}^{2+}$  while blocking neuronal contributions, and similar to our previous experiments (Fig 4), we observed a significant increase in astrocyte  $\text{Ca}^{2+}$  following uncaging of RuBi-DA alone (Fig 5B–C, pink; control). Antagonizing D1 or D2 receptors did not occlude the response to DA release (Fig 5B–C), in accordance with our bath-application data (Fig 3E) and further supporting the idea that DRs are not involved in the recruitment of PFC astrocytes by DA. Next, we tested the contribution of all AR subtypes ( $\alpha 1$ ,  $\alpha 2$  and  $\beta$ ) to DA-mediated astrocyte  $\text{Ca}^{2+}$  activity, and found that only inhibition of  $\alpha 1$ -AR prevented  $\text{Ca}^{2+}$  mobilization after RuBi-DA uncaging (Fig 5B–C). We also measured astrocyte activity using different metrics (raw  $\text{Ca}^{2+}$  events  $dF/F$  [Fig S5A] and percent of field-of-view recruited [Fig S5B]) and found no change from the above results, further supporting the observation that only  $\alpha 1$ -ARs are necessary for the activation of PFC astrocytes by DA. Overall, these *ex vivo* data suggest that fast, volume transmission-like release of DA at physiological concentrations recruits PFC astrocytes via  $\alpha 1$ -ARs.

#### *DA evokes $\text{Ca}^{2+}$ signals in PFC astrocytes via $\alpha 1$ -ARs in vivo*

Our previous results indicate that DA induces fast, transient  $\text{Ca}^{2+}$  signals in prefrontal astrocytes in acute slices. To test whether dopaminergic inputs to the PFC induce astrocyte activity *in vivo*, we carried out dual-color fiber photometry recordings using viral expression of the red-shifted  $\text{Ca}^{2+}$  sensor jR-GECO1b and the DA sensor dLight to monitor both extracellular DA and astrocyte  $\text{Ca}^{2+}$  dynamics (Fig 6A and Fig S6E). Because aversive stimuli such as foot shock (Thierry et al., 1976), tail shock (Abercrombie et al., 1989), and tail pinch (Vander Weele et al., 2018) are known to activate the mesocortical DA system, we used an aversive tail-lift stimulus (Hurst and West, 2010) to increase DA levels in PFC. Using this experimental paradigm and monitoring extracellular DA concentration using dLight, we found that this was indeed the case (Fig 6A, green). jR-GECO1b recordings also showed that there were large astrocyte  $\text{Ca}^{2+}$  transients during the tail-lift procedure (Fig 6A, pink). We aligned the transients from these two recording channels, and saw that the jR-GECO signal closely followed dLight

(Fig 6B–C and Fig S6A). Cross-correlation of the two signals indicated that dLight precedes the jR-GECO signal by 1.4 s (Fig 6D), suggesting that extracellular DA in PFC is a major contributor to the astrocyte  $\text{Ca}^{2+}$  recruitment we observe during this aversive stimulus.

Because aversive stimulation also releases NE in the PFC (Gresch et al., 1994), we next sought to describe any contribution of NE to this close relationship between DA and astrocyte  $\text{Ca}^{2+}$  we observed in the PFC *in vivo*. To do this, we carried out similar dual-color fiber photometry experiments as previously, but after injection of DSP4 (Fig 6E), a toxin that specifically ablates locus coeruleus (LC) projection fibers (Bekar et al., 2008; Ding et al., 2013; Fritschy and Grzanna, 1989), the main source of NE release in PFC. We confirmed that this approach reduced LC fibers in the PFC by performing norepinephrine transporter (NET) immunostaining after DSP4 treatment (Fig 6F), and again compared dLight and jR-GECO dynamics. The amplitude of the DA signals in response to our aversion paradigm were unchanged in astrocytes of NE-depleted mice compared to controls (Fig S6B, left), supporting the selectivity of the toxin used in targeting LC fibers. In addition, while we observed a decrease in astrocyte  $\text{Ca}^{2+}$  amplitude (Fig S6B, right)—in accordance with the documented role of NE in astrocyte  $\text{Ca}^{2+}$  signaling in other brain regions (Bekar et al., 2008; Ding et al., 2013; Gordon et al., 2005; Paukert et al., 2014)—astrocyte  $\text{Ca}^{2+}$  transients co-occurring with dLight transients remained evident after NE-depletion (Fig S6A, middle row). These astrocyte  $\text{Ca}^{2+}$  signals were longer (18 s, Fig S6C), and occurred with longer lag after dLight (2.6 s, Fig S6D) compared to untreated animals (duration 7 s, lag 1.4 s), which may be explained by slower DA uptake in the absence of the NET transporter (Morón et al., 2002; Sesack et al., 1998). Overall, these results indicate that mesocortical DA recruits astrocytes in the PFC when mice are challenged with an aversive stimulation, independent of LC inputs.

Our *ex vivo* experiments indicate that DA effects on PFC astrocytes are mediated by  $\alpha 1$ -AR (Fig 3, Fig 5). To test whether this functional crosstalk between dopaminergic and noradrenergic systems also occurs *in vivo*, we next compared responses to aversive stimulation in mice treated with the LC toxin DSP4 before and after injection of an  $\alpha 1$ -AR antagonist (Prazosin, Fig 6G–H). We found that while dLight signals in response to aversion were maintained after Prazosin (Fig 6G, left), astrocyte  $\text{Ca}^{2+}$  dynamics were significantly reduced (Fig 6G, right) and did not follow DA dynamics (Fig 6H). Together, these data suggest that  $\alpha 1$ -AR signaling accounts for the bulk of the astrocyte  $\text{Ca}^{2+}$  response to DA in the PFC *in vivo*.

#### *DA increases extracellular ATP at PFC astrocytes*

Previous work indicates that DA can stimulate ATP release from astrocytes to modulate synaptic transmission in surrounding neurons in *nucleus accumbens* (Corkrum et al., 2020). To answer whether the  $\alpha 1$ -AR-mediated activation of PFC astrocytes by DA that we observed *in vitro* and *in vivo* also leads to

mobilization of extracellular ATP, we performed 2P acute slice experiments on astrocytes expressing the GPCR-based fluorescent ATP sensor (GRAB<sub>ATP</sub>, Fig 7A) (Wu et al., 2021) and detected extracellular ATP events at astrocytes using AQuA (Fig 7B, G) (Wang et al., 2019). We first determined the response dynamics of the sensor in our experimental setup by bathing on exogenous ATP (50  $\mu$ M, Fig 7B–C), and found that continuous stimulation with ATP led to an increased event rate (Fig 7D), with events whose size matched the territory of an individual astrocyte and could be detected during the entire course of the ATP application (Fig 7E). These data demonstrate that GRAB<sub>ATP</sub> can reliably detect the presence of ATP over the entire astrocyte surface for prolonged periods of time and is suitable for *ex vivo* imaging of extracellular ATP on PFC astrocytes.

After validating this approach to detect extracellular ATP at PFC astrocytes, we next asked whether PFC astrocytes stimulated with DA can lead to extracellular ATP mobilization. We repeated ATP imaging experiments while bath-applying DA (10  $\mu$ M, Fig 7F–H) and blocking neuronal contributions as described above (without PPADS and CGS 15943 to avoid occluding GRAB<sub>ATP</sub> fluorescence changes, see Methods). We found that DA induces mobilization of extracellular ATP (Fig 7H) and an increase in the frequency of ATP events (Fig 7I). These sparse, DA-induced ATP events lasted  $\sim$ 30 s and did not encompass the entire astrocyte territory (Fig 7J). These results indicate that ATP is increased at constrained cellular locations at PFC astrocytes in response to DA. We next carried out the same experiments, but added Doxazosin before each recording, to inhibit  $\alpha$ 1-ARs (Fig 7K). In these experiments, we no longer saw an increase in the frequency of extracellular ATP events after addition of DA (Fig M–N), but the area and duration of the spontaneous events we did see were similar to those observed with addition of DA alone (Fig 7L, O). This result supports the concept that  $\alpha$ 1-ARs are important for DA signaling that leads to ATP increases. Although we do not rule out the contribution of other, non-astrocytic cell types to this phenomenon, this relationship between DA signaling and ATP may contribute to regulation of synaptic transmission in PFC.

## Discussion

### *PFC astrocyte activation relative to behavior*

Recent evidence shows that astrocytes play active roles in brain computation and animal behavior (Kol et al., 2020; Martin-Fernandez et al., 2017; Nagai et al., 2019; Poskanzer and Yuste, 2016), including in the PFC (Mederos et al., 2021). In focusing on astrocytic roles in PFC function, we find that PFC astrocytes differ in neurophysiology from astrocytes in sensory cortices (Fig 1). They are activated with different spatiotemporal patterns of intracellular Ca<sup>2+</sup> (Fig 1), and when animals are exposed to aversive, stressful stimuli (Fig 6), but not in response to locomotion (Fig 1). These results are consistent with PFC neuronal networks being involved in stress processing (Abercrombie et al., 1989; Lammel et

al., 2012; Rosenkranz and Grace, 2001; Thierry et al., 1976; Vander Weele et al., 2018), and with studies demonstrating structural, transcriptomic, and metabolic changes in astrocytes following exposure to acute and chronic stress (Abbink et al., 2019; Bender et al., 2020; Murphy-Royal et al., 2020; Simard et al., 2018). Overall, our results are consistent with previous work showing divergent transcriptomic, morphological, and cellular signaling landscapes in astrocytes of different brain areas (Batiuk et al., 2020; Chai et al., 2017; Khakh and Sofroniew, 2015; Xin et al., 2019), and support the hypothesis that astrocytes may serve specific computational or behavioral functions in PFC.

#### *DA actions on PFC astrocytes: sustained and heterogeneous responses*

Sparser input, faster firing (Lammel et al., 2008), and lower uptake (Sesack et al., 1998) cause greater diffusion and prolonged availability of DA in PFC compared to subcortical areas (Abercrombie et al., 1989; Garris and Wightman, 1994), which, combined with tonic and phasic modes of DA release, results in complex effects on neuronal circuit dynamics (Lohani et al., 2019). While the historical focus of DA signaling in PFC has been on neurons, other cell types such as astrocytes are also well positioned to be reached by these sustained, long-range DA signals and thus contribute to regulation of synaptic transmission in PFC. The ability of astrocytes to respond to dopaminergic signaling with  $\text{Ca}^{2+}$  elevations had been shown in brain areas other than cerebral cortex (Chai et al., 2017; Corkrum et al., 2020; Cui et al., 2016; Fischer et al., 2020; Jennings et al., 2017; Xin et al., 2019). Our study expands this knowledge, demonstrating that astrocytes are capable of sensing DA directly in the PFC, responding with complex  $\text{Ca}^{2+}$  events to both continuous application (Fig 3) and phasic release (Fig 4) of DA. The different dynamics of PFC astrocyte  $\text{Ca}^{2+}$  observed in response to these two modalities of DA delivery suggest a possible mechanism by which astrocytes may discern between tonic and phasic DA signals. Importantly, since we blocked action potentials and neuronally released molecules known to bind GPCRs on astrocytes in our *ex vivo* experiments, our data demonstrate that PFC astrocytes respond to DA independently of neuronal activation by DA, suggesting that astrocytes actively contribute to modulation of PFC activity via DA.

Our uncaging data (Fig 4) show that, even in the absence of neuronal responses to DA, the rapid release of physiological concentrations of DA recruits astrocyte responses within seconds, which are sustained for tens of seconds in the majority of cells, but not all. Individual astrocyte responses, rather than population-wide activity, demonstrate that the extent of subcellular locations engaged in  $\text{Ca}^{2+}$  signaling following DA release within individual cells differs across PFC astrocytes. These observations suggest that astrocytes may be involved in regulation of sustained activity or network dynamics, as well as contribute to the local computation of PFC circuitry in a cell-specific manner, as shown previously in other brain areas (Martín et al., 2015; Martin-Fernandez et al., 2017).

### *DA actions on PFC astrocytes: receptors and signaling pathways*

Our results demonstrate that DA acting on PFC astrocytes recruits  $\text{Ca}^{2+}$  (Fig 3–4) rather than cAMP (Fig 2). These data are in contrast with previous neuronal research showing that DA activates the  $G_s/G_i$ -cAMP pathways canonically ascribed to D1 and D2 receptors (Lee et al., 2021; Muntean et al., 2018; Nomura et al., 2014; Yapo et al., 2017), but in agreement with previous astrocytic work from other brain areas which have shown that DA activates the  $G_q$ -IP<sub>3</sub>-  $\text{Ca}^{2+}$  pathway (Chai et al., 2017; Corkrum et al., 2020; Cui et al., 2016; Fischer et al., 2020; Jennings et al., 2017; Xin et al., 2019). Together, these results may suggest differential expression of components of the signaling machinery across brain cell types. However, the possibility supported by our pharmacology data (Fig 3, 5–6) is that the lack of cAMP mobilization is due to DA acting on PFC astrocytes exclusively through  $\alpha 1$ -AR—the only  $G_q$ -coupled receptor across all DR and AR subtypes—even though PFC astrocytes do express D1 and D2 receptors (Fig 2). Indeed, our data demonstrating that PFC astrocytes respond to DA with fast, transient  $\text{Ca}^{2+}$  mobilization mediated by  $\alpha 1$ -ARs differs from previous work on astrocytes in other brain regions, in which DA can induce  $\text{Ca}^{2+}$  responses via DRs (Corkrum et al., 2020; Fischer et al., 2020; Jennings et al., 2017). However, our data that astrocytes sense DA via cell-surface  $\alpha 1$ -ARs, and not DRs, is consistent with studies of neuronal activation by DA also report that DRs agonists or antagonists are unable to reproduce or prevent the effects of DA (Cilz et al., 2014; Cornil and Ball, 2008; Cornil et al., 2002; Guiard et al., 2008; Marek and Aghajanian, 1999; Nicola and Malenka, 1997; Özkan et al., 2017). Further, our unexpected finding could help reconcile some apparently contradictory findings in the astrocyte literature whereby different methods (DA versus D1/D2 agonists, or blockade of DA with DR antagonists) for DA activation lead to contrasting results even within brain regions (Corkrum et al., 2020; D’Ascenzo et al., 2007). For instance, the documented dorso-ventral or layer-specific gradients of VTA/LC innervation or DR/AR expression in the hippocampus (Edelmann and Lessmann, 2018) could have influenced the pharmacology of cellular responses observed by Jennings *et al.*, whereby lower local expression of DRs in *stratum lacunosum-moleculare* could have allowed AR-mediated DA responses to take over and explain the lack of sensitivity of DA-induced responses to DR antagonists. Similarly, because the transcriptomic, morphological, and cellular signaling landscape of astrocytes can diverge in different cortical layers or brain areas (Batiuk et al., 2020; Chai et al., 2017; Lanjakornsiripan et al., 2018; Xin et al., 2019), region- or subregion-specific patterns of innervation and receptor expression could favor different mechanisms of DA activation—via DRs or ARs—and explain the lack of activation by D1/D2 agonists observed by some studies (Chai et al., 2017; D’Ascenzo et al., 2007), as well as the lack of inhibition by DRs antagonists found by others (Jennings et al., 2017).

### *What is the adaptive role of DA/ $\alpha$ 1-AR promiscuity?*

An important implication of our findings is that DA signaling *ex vivo* (Fig 3, 5) and *in vivo* (Fig 6) is subject to receptor promiscuity. This result is supported by previous research reporting that the effects of DA on neurons could not be reproduced using DA-selective agonists (Cilz et al., 2014; Nicola and Malenka, 1997; Özkan et al., 2017), or could be prevented by  $\alpha$ -AR, but not DR, antagonists (Cilz et al., 2014; Cornil et al., 2002; Guiard et al., 2008; Marek and Aghajanian, 1999; Özkan et al., 2017). Further, many levels of interactions between the dopaminergic and noradrenergic systems have been documented in the PFC: DA and NE are co-released by LC fibers (Devoto et al., 2005), DA uptake is accomplished mainly by NET (Morón et al., 2002) due to low DAT expression in PFC (Sesack et al., 1998), and sub- or supra-threshold stimulation of both systems leads to detrimental outcomes on PFC performance (Arnsten et al., 2012). Together, this evidence supports the idea that DA may interact with the noradrenergic system at the receptor and signal transduction level on PFC astrocytes. However, despite likely acting through the same astrocytic receptors, DA and NE show markedly different  $Ca^{2+}$  mobilization signatures: DA evokes events that are small in amplitude and duration, but occur at high frequency and are prolonged over time (Fig 3), while previous work shows that NE causes strong events of big amplitude and short duration (Pankratov and Lalo, 2015). Thus, the DA-AR crosstalk described in the present study does not implicate losing information about where a given extracellular signal originated from, as astrocytes may still be able to implement different computations and activate different effects downstream of specific inputs, likely through different combinations of receptors recruited and their stoichiometry and position relative to signal transducers and effectors.

Although VTA-DA and LC-NE traditionally play dissociable roles in the brain, evidence of a functional relevance of DA/NE co-release by LC fibers to memory consolidation in the hippocampus (Kempadoo et al., 2016; Smith and Greene, 2012; Takeuchi et al., 2016) could suggest that DA/NE co-release in the PFC (Devoto et al., 2005) might also be relevant to specific prefrontal cognitive processes. However, our data shows that substantial PFC DA dynamics are maintained in the PFC of DSP4-treated mice that lack LC innervation (Fig 6), in accordance with previous work *in vivo* (Berger et al., 1974; Vander Weele et al., 2018). Nevertheless, the specific functional effects of DA/NE co-release in the PFC remain to be explored, and recent advances in extracellular neurotransmitter imaging probes (Feng et al., 2019; Muller et al., 2014; Patriarchi et al., 2018, 2020; Sun et al., 2018) will help understand how astrocytes, as well as neurons, are regulated differentially by these two neuromodulators. For instance, is the release of VTA-DA and LC-DA in PFC driven by similar or divergent behavioral stimuli, leading then to mutual reinforcement or rather reciprocal modulation of segregate inputs? Does co-release of DA/NE from LC fibers in the PFC mediate specific aspects of PFC executive functions? On the other hand, given DA availability in PFC is prolonged compared to that of NE (Devoto et al., 2005) thus

leading to greater spatial diffusion, do LC-DA and LC-NE reach similar or different cellular targets, and with what temporal mismatch? In both scenarios, astrocytes are well positioned to detect both temporally segregated or coincident DA/NE signals, as they express receptors for both neurotransmitters whose stimulation generates distinctive cellular responses. Further studies are needed to address the extent of the crosstalk between the DA and NE system, both within astrocytes and across brain cell types, as well as its implications on brain function and animal behavior.

How this receptor/neuromodulator promiscuity originates at the receptor level is another exciting follow-up area. For example, does DA bind directly to  $\alpha 1$ -ARs and stimulate  $\text{Ca}^{2+}$  independently from DRs? Or does DA induce a physical interaction between the bound DR and  $\alpha 1$ -AR, which then drives downstream  $\text{Ca}^{2+}$  mobilization? While radioligand binding studies indicate that non-specific interaction of DA with  $\alpha 1$ -AR only occurs at sub-millimolar concentrations (Proudman and Baker, 2021; Steinberg and Bilezikian, 1982) (much higher than those used in the present experiments), D1 and  $\alpha 1$ AR colocalize on PFC dendrites and have been suggested to undergo co-trafficking (Mitrano et al., 2014). In addition, mounting evidence from co-immunoprecipitation, BRET/FRET sensors and proximity-ligation assays support the idea that DRs can form functional heteromeric complexes with ARs and other class A GPCRs (Azdad et al., 2009; Bonaventura et al., 2014; González et al., 2012; Kolasa et al., 2018; Lee et al., 2004; Moreno et al., 2014; Navarro et al., 2018; Pelassa et al., 2019; Rebois et al., 2012; Trifilieff et al., 2011; Valle-León et al., 2021; Zhu et al., 2020), although evidence against the existence of DR heteromers *in vivo* also exists (Frederick et al., 2015).

Many clinical drugs used to treat psychiatric disorders such as depression, anxiety, ADHD, and schizophrenia target multiple monoamine systems, and can have severe side effects and low remission rates (Stanford and Heal, 2019). For instance, astrocytes have been linked to ADHD (Nagai et al., 2019), and methylphenidate—a first-line therapy for ADHD—increases both DA and NE concentration by blocking DAT and NET (Berridge et al., 2006). Our results here highlight open questions about treatments like these: are both neuromodulators needed for the therapeutic outcomes of methylphenidate, and are they both involved in its adverse effects? Do DA and NE act differently on neurons or non-neuronal cells? Are both DRs and ARs required to transduce DA signals in astrocytes, and if so would drugs that specifically target this interaction achieve better outcomes and minimize side effects? Clarifying the nature of the interaction between dopamine and ARs will be key for understanding the implications of drug treatment in conditions where both catecholamine systems are involved.

#### *Prefrontal DA, astrocytes and ATP*

Extracellular ATP is an important regulator of brain circuits that can be released by astrocytes in other brain areas in response to DA (Corkrum et al., 2020) and other neurotransmitters (Gordon et al.,

2005; Lalo et al., 2014; Pougnet et al., 2014) and lead to a generalized depression of synaptic transmission (Corkrum et al., 2020; Martin-Fernandez et al., 2017; Pascual et al., 2005; Zhang et al., 2003). PFC astrocytes are capable of ATP release (Cao et al., 2013), and, consistent with this, our experiments show regulation of extracellular ATP in response to DA (Fig 7). In our experimental conditions, the mobilization of ATP is delayed relative to DA, which could potentially tie this function of astrocytes to sustained activity in PFC during delay periods of working memory tasks. DA actions on both pyramidal cells and interneurons influence recurrent activity in PFC microcircuits (Goldman-Rakic, 1995), as well as excitatory/inhibitory balance (Gao and Goldman-Rakic, 2003; Gao et al., 2003), which are fundamental for the generation and maintenance of sustained activity. Because ATP depresses transmission, DA may favor suppression of PFC activity through astrocyte-derived ATP. Our ATP imaging shows that DA acting on PFC astrocytes induces spatially restricted patterns of extracellular ATP, suggesting that astrocytes could depress activity of specific PFC synapses located within their territories. Cell-type specific activity in PFC occurs during specific cognitive tasks (Kamigaki and Dan, 2017; Kim et al., 2016; Pinto and Dan, 2015), and cell-type specificity in astrocyte-neuron interactions has been reported in other brain areas (Martín et al., 2015; Martin-Fernandez et al., 2017), so future experiments could explore whether PFC astrocytes regulate ATP at defined pyramidal or interneuron subtypes, or subsets of synapses, to coordinate specific PFC microcircuits and influence cognitive function.

### *Conclusion*

Overall, the present work contributes to the fields of PFC, DA, and astrocyte research. Our data indicate that prefrontal astrocytes have distinct features compared to sensory cortex astrocytes, and respond to DA with non-canonical  $\text{Ca}^{2+}$  mobilizations that occur via  $\alpha 1$ -AR. Future work will address how PFC DA acting on astrocytes contributes to network dynamics and executive function, as well as the molecular basis and functional consequences of the crosstalk between DA and adrenergic receptors.

### **Acknowledgements**

The authors are grateful to members of the Poskanzer lab for helpful discussions, in particular Michelle Cahill for discussions about *ex vivo* analysis. We thank the Bender lab (UCSF) for reagents and assistance with PFC slicing, the Yuste lab (Columbia University) for assistance with reagents, Victoria Cheung in the Feinberg lab (UCSF) for help with initial fiber photometry recordings, Hajime Hirase (RIKEN, University of Copenhagen) for Pink Flamindo virus, and Jennifer Thompson for essential administrative support. K.P. is supported by NIH R01NS099254, NIH R01MH121446, NIH R21DA048497, and NSF CAREER 1942360. S.P. is supported by the EU under the Horizon 2020 Marie Skłodowska Curie

Actions project ASTRALIS, GA 839561. M.R. was supported by the UCSF Genentech Fellowship. R.E. is a member of CONICET.

### **Author Contributions**

K.P and S.P. conceived and designed the study, and wrote the manuscript with input from the other authors. S.P. carried out *ex vivo* imaging and fiber photometry experiments and analyzed all data. S.Y. performed the *in vivo* 2P imaging experiments in PFC through GRIN lenses, *post hoc* immunostaining, and immunostaining/analysis of dopaminergic receptors. D.W. performed the fiber photometry experiments. C.T. performed the *ex vivo* GRAB<sub>ATP</sub> experiments. M.R. carried out the *in vivo* 2P imaging experiments of V1. V.T. carried out immunostaining of *post hoc* tissue. Z.W. and Y.L. developed, tested, and provided GRAB<sub>ATP</sub>. R.E. provided critical support related to the RuBi-DA.

### **Declaration of Interests**

The authors declare no competing interests.

## Figures and Figure Legends

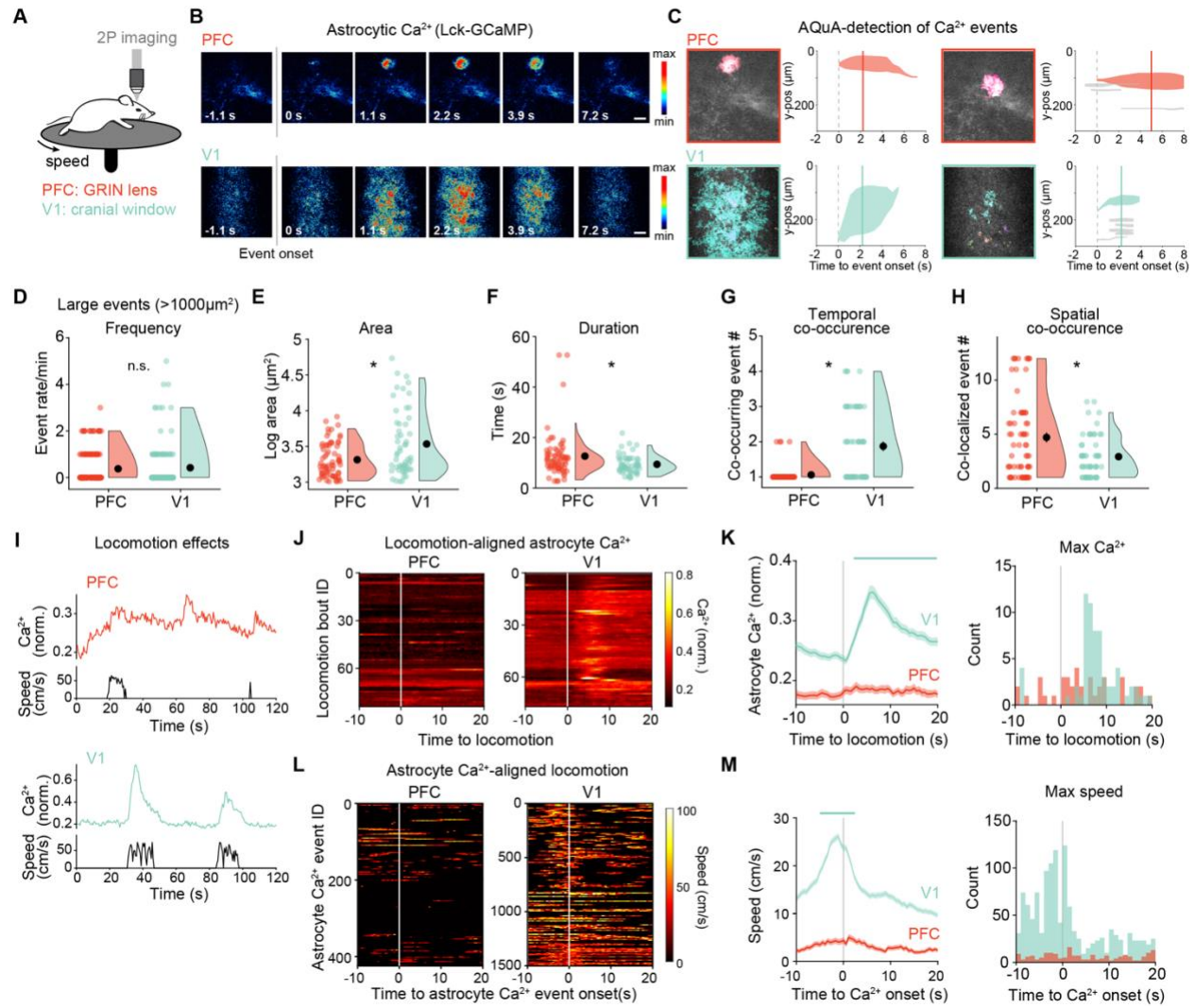


**Figure 1: PFC astrocytes exhibit region-specific Ca<sup>2+</sup> activity.** (A) Experimental setup for head-fixed 2P imaging of astrocyte Ca<sup>2+</sup> in PFC (via GRIN lens) or V1 (cranial window) in vivo. (B) Representative frames of pseudocolored astrocytic GCaMP6f fluorescence in PFC (top) or V1 (bottom), relative to Ca<sup>2+</sup> event onset. Scale bars = 50 μm. (C) Two examples of large AQuA-detected Ca<sup>2+</sup>-events each in PFC (red, top) and V1 (green, bottom). Fields-of-view = 300 x 300 μm<sup>2</sup>. To the right of each image is the corresponding timecourse of all detected events within 10 s, with the time of onset of the largest event at t = 0 and the solid line indicating the frame displayed at left. Events <1000 μm<sup>2</sup> are in gray. (D–H) Large (>1000 μm<sup>2</sup>) astrocyte Ca<sup>2+</sup>-event features vary between brain regions. Events occur at similar rates in PFC and V1 (D), but in PFC are (E) smaller and (F) longer than in V1. Events in PFC (G) co-occur with other events less than in V1, but (H) tend to repeat more at the same spatial location. Data shown as all bins/events (colored dots), 5<sup>th</sup>–95<sup>th</sup> percentile distribution (violins), and mean ± sem (black dots and error bars). Event rate (min<sup>-1</sup>): 0.38±0.05 (PFC), 0.42±0.08 (V1); area (μm<sup>2</sup>): 2422±190 (PFC), 6639±1346 (V1); duration (s): 12.6±1.1 s (PFC), 9.4±0.5 s (V1); temporal co-occurrence: 1.06±0.03 (PFC), 1.87±0.13 (V1); spatial co-occurrence: 4.7±0.5 (PFC), 2.9±0.3 (V1). Wilcoxon rank-sum test; \*, p < 0.05; p = 0.6288 (frequency), p = 0.0122 (area), p = 0.0116 (duration), p < 10<sup>-4</sup> (co-occurring), p = 0.0340 (co-localized). PFC: n = 180 60-s bins, 68 events, 4 mice; V1: n = 130 60-s bins, 55 events, 3 mice. (I–M)

Locomotion does not induce population-wide astrocyte  $\text{Ca}^{2+}$  in PFC. (I) Example time course of normalized astrocyte  $\text{Ca}^{2+}$  (colored trace, top) and corresponding mouse speed (black, bottom) in PFC and VI. (J–K) Astrocyte  $\text{Ca}^{2+}$  traces aligned to the onset of locomotion ( $t = 0$ ), shown as heatmaps for all recordings (J), average traces  $\pm$  sem (K, left) and binned distribution of maximum  $\text{Ca}^{2+}$  change (K, right). In (K), line above mean traces indicates significant change from average  $\text{Ca}^{2+}$  at  $t < 0$ . Shuffle test, 10000 pair-wise shuffles;  $p < 0.01$ , Bonferroni correction for multiple comparisons. PFC:  $n = 84$  bouts, 4 mice; VI:  $n = 77$  bouts, 3 mice. (L–M) Animal speed aligned to onset of astrocyte  $\text{Ca}^{2+}$  events ( $t = 0$ ), shown as heat map for all recordings (L), average traces  $\pm$  sem (M, left), and binned distribution of maximal speed (M, right). In (M), line above mean traces indicates significant increase above the average speed for the entire window. Shuffle test, 10000 pair-wise shuffles;  $p < 0.01$ , Bonferroni correction for multiple comparisons. PFC:  $n = 424$  events, 4 mice; VI:  $n = 1501$  events, 3 mice.

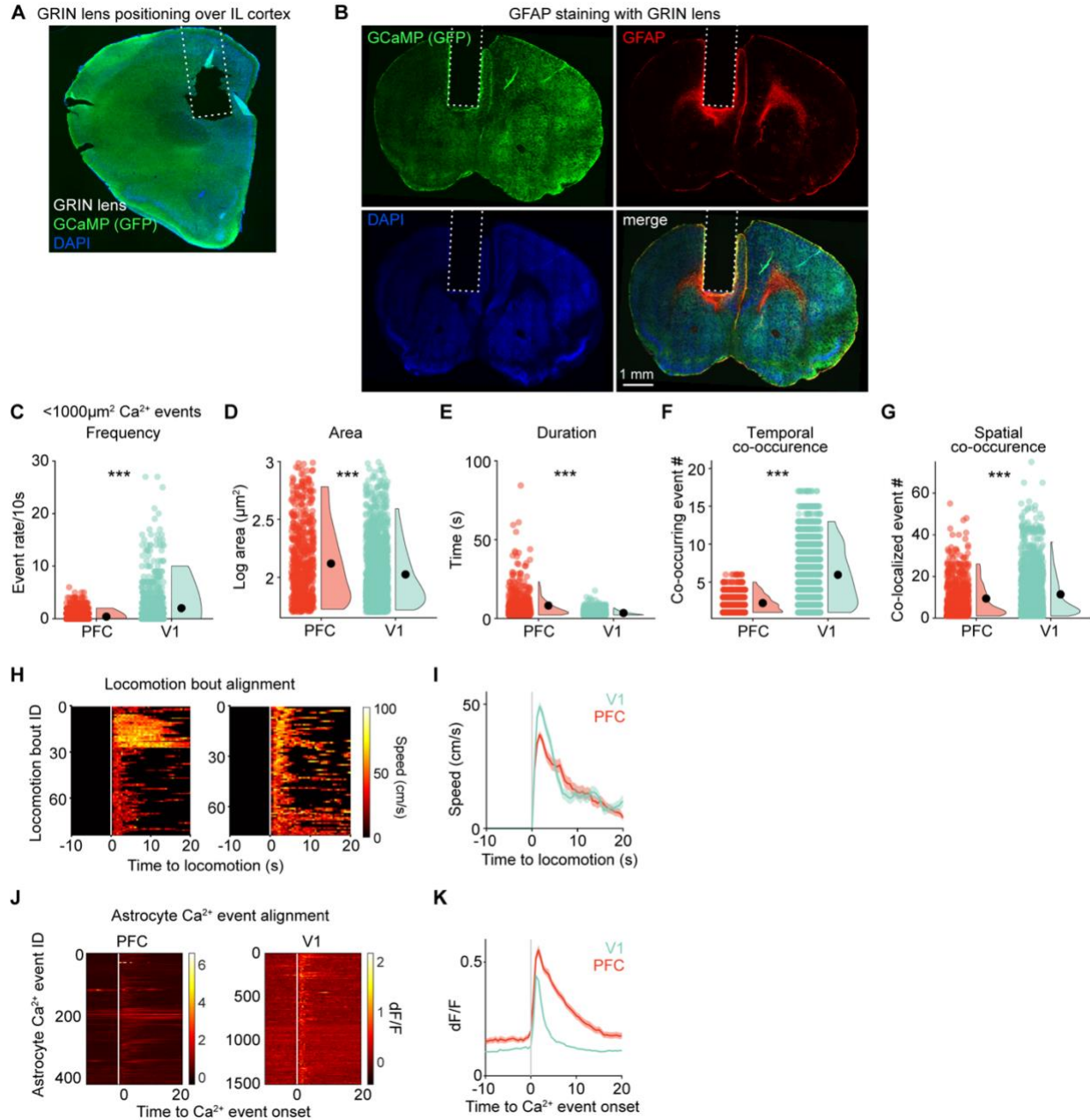


**Figure S1, related to Fig. 1.** (A) GRIN lens implant location in PFC was confirmed by fixation and sectioning (~2 mm anterior from Bregma), immunostaining to visualize astrocytic expression of Lck-GCaMP (green) and DAPI (blue) for nuclei. (B) GFAP (red), astrocytic Lck-GCaMP (green), and nuclei staining (DAPI, blue) were used to assess astrocyte reactivity around implanted GRIN lenses. (C–G) Small ( $<1000\mu\text{m}^2$ ) astrocyte  $\text{Ca}^{2+}$ -event features also vary between brain regions. Small events occur at lower rates in PFC (C), but are (D) larger and (E) longer than those in V1. Small events in PFC (F) co-occur with other events less than in V1, but (G) tend to repeat less at the same spatial location. Data shown as all bins/events (colored dots), 5<sup>th</sup>–95<sup>th</sup> percentile distribution (violins), and mean  $\pm$  sem (black dots and error bars). Wilcoxon rank-sum test; \*\*\*,  $p < 10^{-5}$ . PFC:  $n = 1486$  60-s bins, 593 events, 4 mice; V1:  $n = 780$  60-s bins, 1561 events, 3 mice. (H–I) Animal speed (cm/s) aligned to start of locomotion bouts ( $t = 0$ ), shown as heat map for all locomotion bouts (H) and average traces  $\pm$  sem (I). (J–K) Astrocyte  $\text{Ca}^{2+}$  traces (dF/F) aligned to the onset of the AQuA-detected  $\text{Ca}^{2+}$  events ( $t = 0$ ), shown as heatmaps for all events (J) and average traces  $\pm$  sem (K).

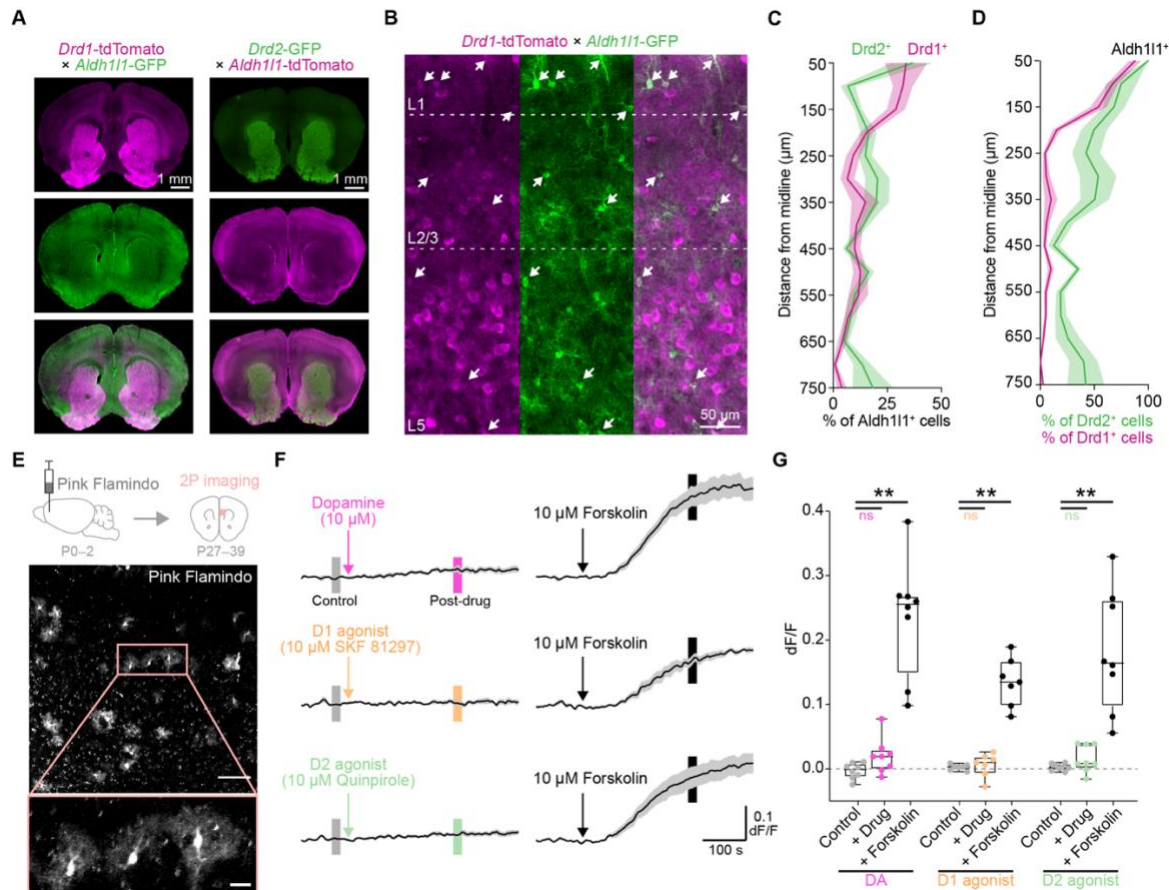


**Figure 2: D1 and D2 receptors are expressed by PFC astrocytes but do not recruit G<sub>s</sub>/G<sub>i</sub> pathways.** (A) Transgenic crosses to identify co-expression of D1 (left column, top) or D2 receptors (right column, top) with the astrocytic marker *Aldh11* (middle row). Whole-brain coronal sections ~1.6 mm anterior to Bregma. (B) Example of marker colocalization in PFC of a *Drd1*-tdTomato × *Aldh11*-GFP mouse. Arrowheads indicate astrocytes co-expressing D1 (magenta) and *Aldh11* (green). Boundaries between cortical layers indicated by dashed lines for reference. (C–D) Percentage of (C) *Aldh11*<sup>+</sup> astrocytes expressing D1 (*Drd1*<sup>+</sup>, magenta) and D2 (*Drd2*<sup>+</sup>, green), and of (D) *Drd1*<sup>+</sup> (magenta) and *Drd2*<sup>+</sup> (green) cells that co-express *Aldh11* in PFC. Data shown as mean ± sem; n = 3 sections/mouse, 3 (D1) and 2 (D2) mice. (E) Experimental schematic for 2P imaging of astrocytic cAMP in acute PFC slices. Micrographs show Pink Flamindo expression in entire imaged field-of-view (top), and 3 zoomed-in cells with clear astrocyte morphology (bottom). Scale bars = 100 μm (top) and 20 μm (bottom). (F) Dopamine receptor agonists (colors) do not mobilize whole-cell cAMP signaling in PFC astrocytes. Adenylate cyclase activator Forskolin (black) was used in the same slices to confirm Pink Flamindo activity. Neuronal action potentials and neuron-to-astrocyte communication were prevented using TTX and a drug cocktail (see Methods). Vertical boxes on traces indicate 20-s windows used for quantification in (G). Traces shown as slice averages ± sem of whole-cell changes in Pink Flamindo intensity (dF/F); n = 110–180 cells, 7–8 slices, 7–8 mice. (G) Quantification of (F) at time-points indicated by small vertical boxes, shown as box plots indicating mean and 10<sup>th</sup>–90<sup>th</sup> percentile, and error bars indicating minima and maxima. Slice mean ± sem (Control, +Drug, +Forskolin): -0.003±0.004, 0.02±0.01, 0.24±0.03 (DA); 0.003±0.002, 0.006±0.007, 0.13±0.01 (D1); 0.003±0.002, 0.016±0.007, 0.18±0.03 (D2). Friedman test after Levene test; n.s., p > 0.05, \*\*, p < 0.01; not shown on graph are comparison between Drug and Forskolin (p < 0.05 for all agonists), and comparisons within conditions (controls, Drugs, or Forskolins; one-way Anova or Kruskal-Wallis after Levene test, all p > 0.05); n = 110–180 cells, 7–8 slices, 7–8 mice.

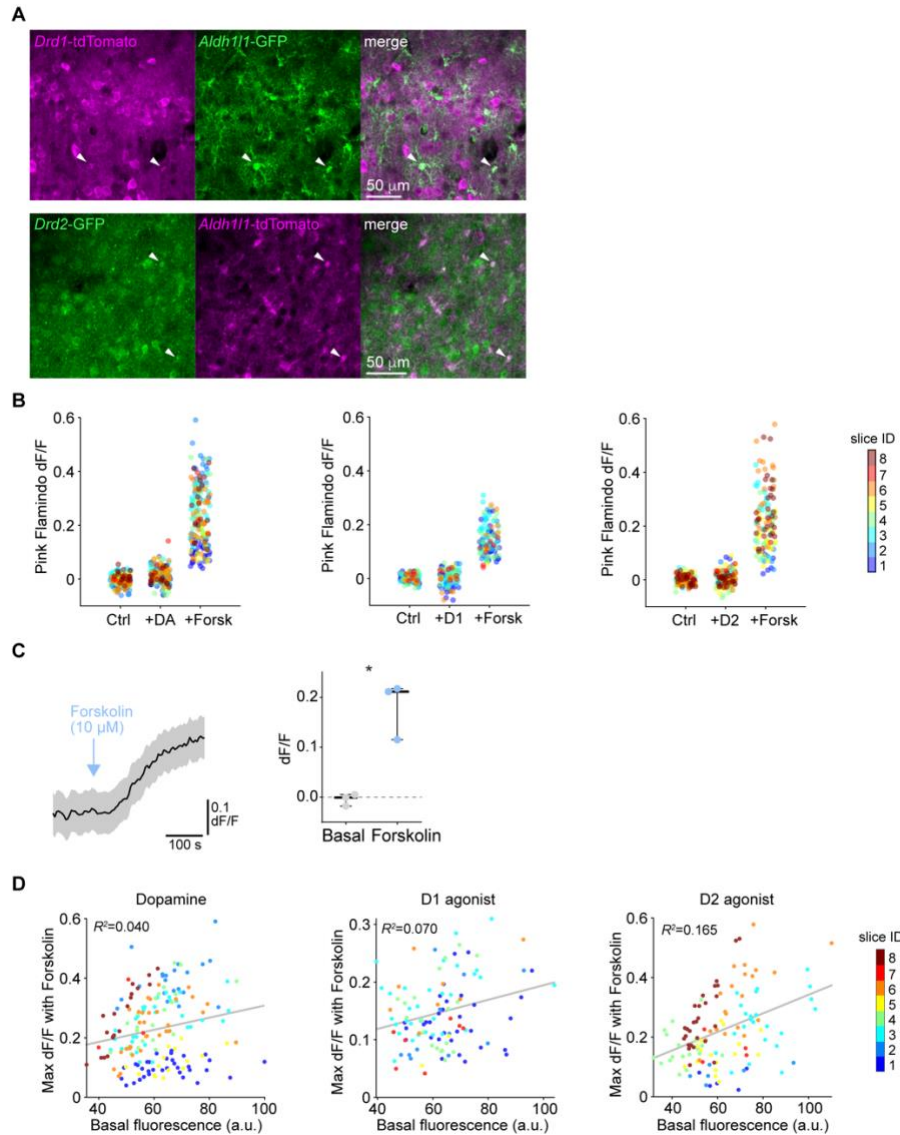


**Figure S2, related to Fig. 2.** (A) Examples of high magnification (20x) micrographs from PFC of (top) *Drd1*-tdTomato x *Aldh111*-GFP and (bottom) *Drd2*-GFP x *Aldh111*-tdTomato mice to demonstrate colocalization and cell morphology. Arrowheads indicate cells co-expressing either receptor and Aldh111. (B) Fluorescence change from baseline for all analyzed cells, with colors indicating individual slices, to highlight no evident clustering of cells within individual slices. For the “+DA” condition, there is no evident separation of cells into two separate clusters, indicating that DA does not activate D1 ( $G_s$  pathway) and D2 receptors ( $G_i$  pathway) in different cells. Corresponding slice averages are shown in Fig 2G. (C) Adenylate cyclase activator Forskolin mobilizes cAMP in naïve slices, *i.e.* not treated with TTX and the drug cocktail to block neurons, at similar levels to those observed in treated slices (right; + Forskolin =  $0.18 \pm 0.03$  dF/F). Data shown as (left) mean traces  $\pm$  sem and (right) slice averages  $\pm$  sem of whole-cell Pink Flamindo fluorescence (dF/F) before (basal) and after Forskolin. Paired t-test; \*,  $p = 0.036$ ;  $n = 58/144$  cells, 3 slices and mice. Scale = 100 s, 0.1 dF/F. (D) Astrocytic response to maximal adenylate cyclase stimulation correlates weakly with cAMP reporter expression (Pink Flamindo basal fluorescence, arbitrary units). The observed variability in maximal cAMP concentrations in PFC astrocytes may reflect different signaling capabilities of individual astrocytes (*e.g.*, differential expression levels of AC subtypes, phosphodiesterases, *etc.*). Data are shown as cells (dots), colors indicate individual slice IDs. Pearson’s coefficients ( $r^2$ ) of linear correlation fits are indicated;  $p$ -values < 0.007.

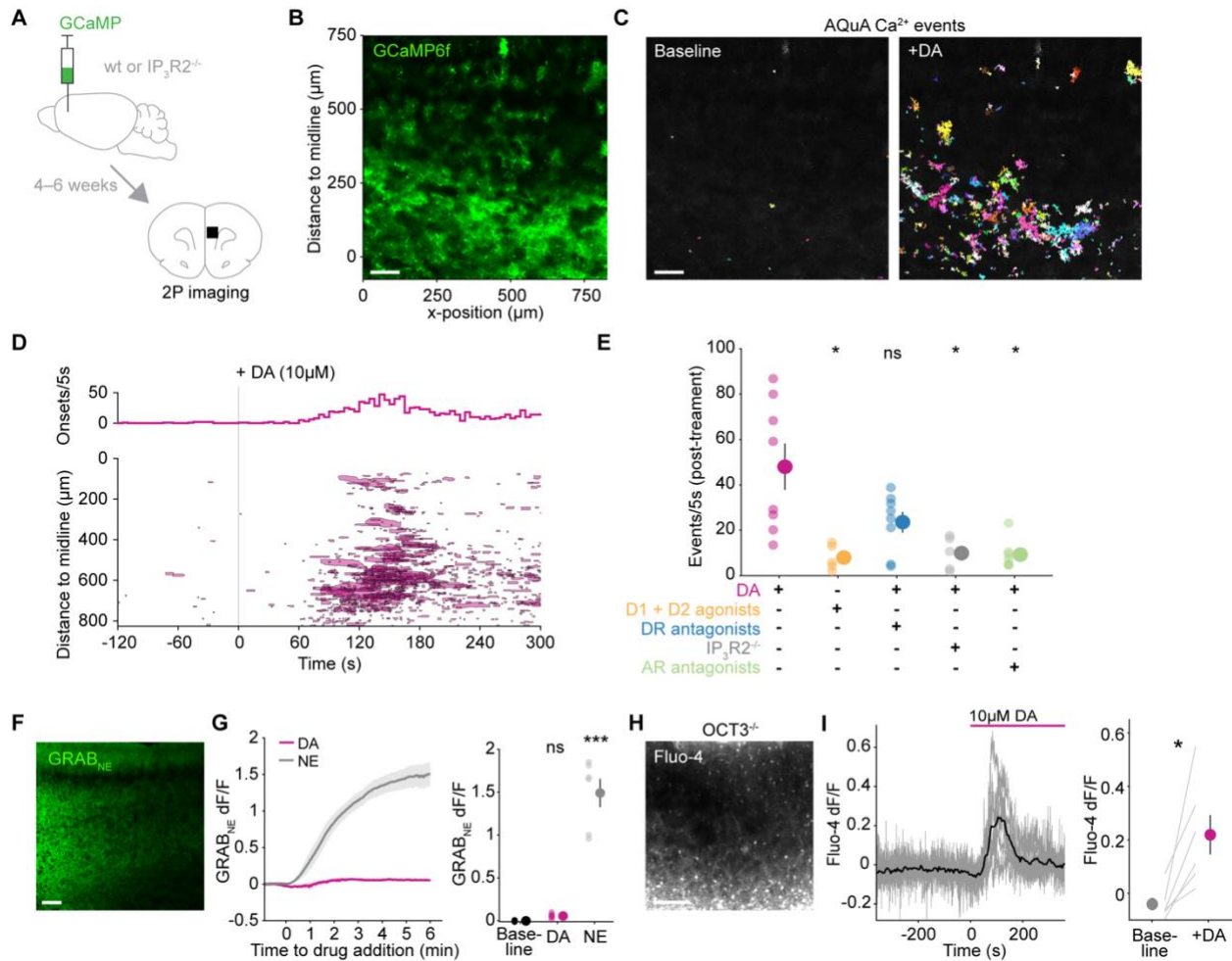


**Figure 3: DA mobilizes astrocytic  $\text{Ca}^{2+}$  in PFC slices via cell-surface adrenergic receptors. (A)**

Experimental strategy for 2P imaging of astrocytic  $\text{Ca}^{2+}$  in acute PFC slices. **(B)** Representative micrograph of *GfaABC1D*-GCaMP6f expression in imaged area of PFC. Note y-axis measurements of distance to slice midline, which are used for spatial plots in **(D)**. Scale bar = 100  $\mu\text{m}$  throughout figure **(C)** All AQuA-detected  $\text{Ca}^{2+}$  events 0–60 s before (left) and 90–150 s after bath-application of DA (right) from same slice as in **(B)**. Colors represent individual events. **(D)** Time course of all  $\text{Ca}^{2+}$  events detected over the entire recording of slice in **(B–C)** and event onset rate (top) relative to 10  $\mu\text{M}$  DA ( $t = 0$ ). Shaded areas represent approximate event size and mean event y-position over time. **(E)** Astrocytic  $\text{Ca}^{2+}$ -event rate (count/5 s) in PFC slices after treatment with indicated drugs. Treatment with both D1 and D2 agonists SKF38393 and Quinpirole (yellow) did not have the same effect of inducing increased  $\text{Ca}^{2+}$  events as DA (magenta). Blocking both D1 and D2 receptors with DRs antagonists SCH23390 and Sulpiride during DA application (blue) failed to occlude astrocyte activation by DA, whereas the effect of DA alone was significantly reduced in  $\text{IP}_3\text{R}2^{-/-}$  mice (grey). Likewise, non-selective  $\alpha$ - and  $\beta$ -AR antagonists Phentolamine and Propranolol (green) significantly reduced the astrocytic  $\text{Ca}^{2+}$  response to DA. Data shown as slices (transparent dots) and corresponding mean  $\pm$  sem (solid dot and error bar):  $48.0 \pm 10.2$  (DA);  $8.0 \pm 2.5$  (D1/D2 ago.);  $23.6 \pm 4.6$  (DR antag.);  $9.9 \pm 3.3$  ( $\text{IP}_3\text{R}2^{-/-}$ );  $9.3 \pm 2.5$  (AR antag.). Kruskal-Wallis test after Levene test; \*,  $p < 0.05$  compared to DA condition; all other comparisons between conditions (not shown),  $p > 0.79$ ;  $n = 5\text{--}8$  slices, 4–8 mice. **(F)** Example of tissue-wide expression of  $\text{GRAB}_{\text{NE}}$  for 2P imaging in an acute PFC slice. **(G)** DA is not metabolized to NE in PFC slices, as indicated by  $\text{GRAB}_{\text{NE}}$  dynamics. Left: trace means  $\pm$  sem relative to either DA or NE addition at  $t = 0$ . Right: slices (dots) and mean  $\pm$  sem (dot with error bar) of 20-s  $\text{GRAB}_{\text{NE}}$  dF/F averages at baseline (black), or 6 min after 10  $\mu\text{M}$  DA (magenta) and 10  $\mu\text{M}$  NE (grey):  $-0.002 \pm 0.003$  (Baseline);  $0.055 \pm 0.012$

(DA);  $1.490 \pm 0.165$  (NE). Kruskal-Wallis test after Levene test; \*\*\*,  $p < 0.001$  relative to baseline;  $n = 6$  slices, 4 mice. **(H)** Example acute slice from OCT3<sup>-/-</sup> mice with deficient DA uptake, loaded with the Ca<sup>2+</sup> indicator Fluo-4. **(I)** Somatic Ca<sup>2+</sup> signals in response to bath-applied DA are present in PFC astrocytes in the OCT3<sup>-/-</sup> background. Left: mean trace (black) and slice average traces of active cells (grey) relative to addition of 10  $\mu$ M DA at  $t = 0$ . Right: slice averages (lines) and corresponding mean  $\pm$  sem (dots and error bars) of Fluo-4 dF/F extracted from traces on left at either 100-s before (Basal) or after DA (+DA):  $-0.04 \pm 0.02$  (Baseline);  $0.22 \pm 0.08$  (+DA). Paired t-test after Anderson-Darling test; \*,  $p < 0.05$ ;  $n = 138$  active cells, 6 slices, 3 mice.

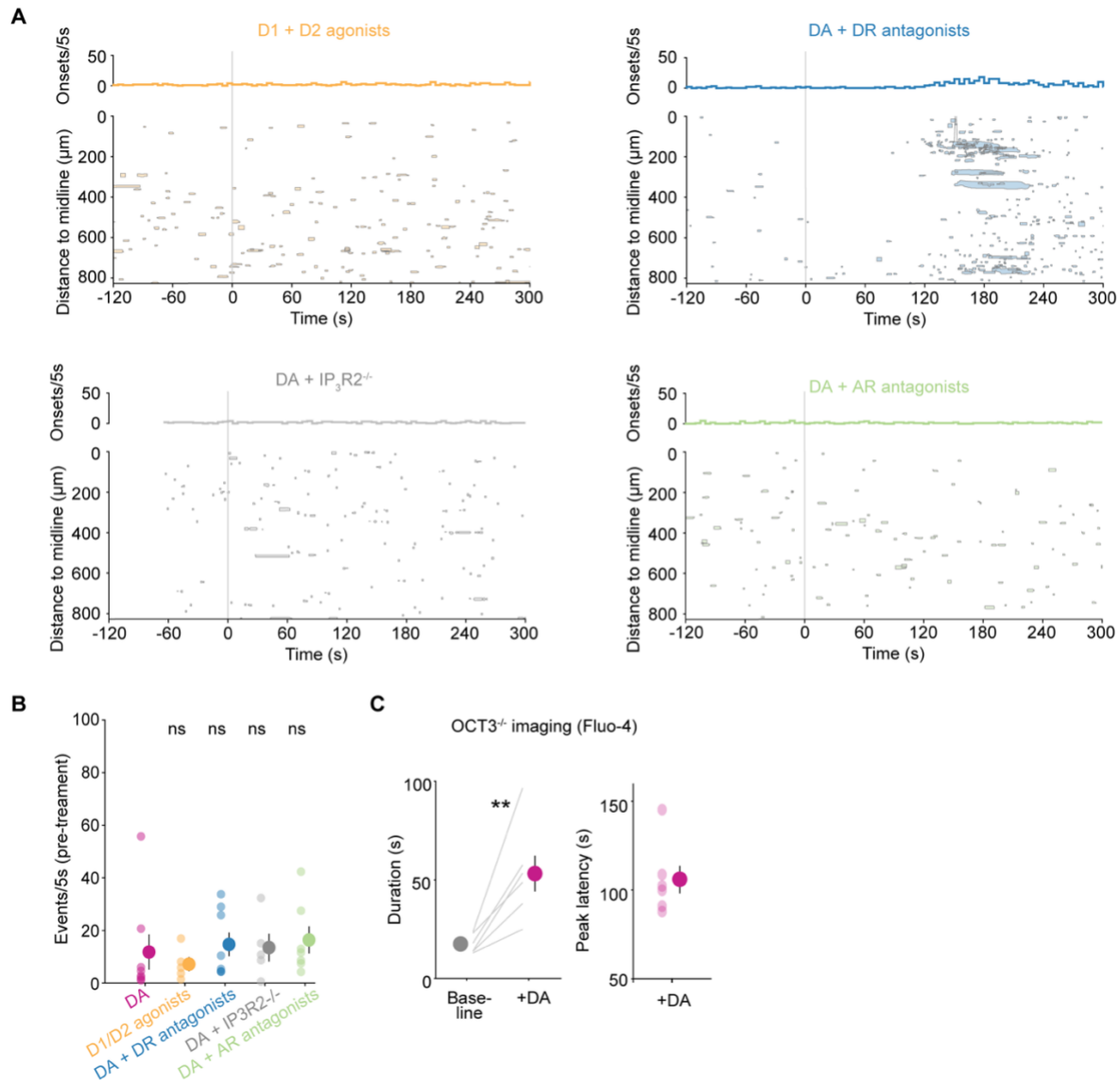


**Figure S3, related to Fig. 3.** (A) Time course of all astrocyte  $\text{Ca}^{2+}$  events detected in PFC slices relative to D1/D2 agonists application (SKF38393/Quinpirole, top left), or relative to DA application in D1/D2 antagonists (SCH23390/Sulpiride, top right), in  $\text{IP}_3\text{R2}^{-/-}$  mice (bottom left), or in  $\alpha$ -/ $\beta$ -AR antagonists (Phentolamine/Propranolol, bottom right). Rate of event onset (counts in 5-s bins) is displayed on top of each graph. Shaded areas represent approximate event size and mean y-position of the event over time. (B) No difference in pre-treatment event rate (count/5 s) for all slices and conditions shown in Fig. 2E. Event rate was calculated over a 60-s period before treatment with DA or D1/D2 agonists (as indicated by x-axis labels). Data shown as all slices (transparent dots) and corresponding mean  $\pm$  sem (solid dot and error bar) for each condition:  $11.8 \pm 6.7$  (DA);  $7.2 \pm 2.7$  (D1/D2 ago.);  $14.7 \pm 4.5$  (DR antag.);  $13.5 \pm 5.3$  ( $\text{IP}_3\text{R2}^{-/-}$ );  $16.4 \pm 5.2$  (AR antag.). One-way Anova after Levene test;  $p = 0.829$ ;  $n = 5$ – $8$  slices,  $4$ – $8$  mice. (C) Average duration (left) and latency (right) of astrocytic somatic  $\text{Ca}^{2+}$  transients in slices from  $\text{OCT3}^{-/-}$  mice imaged using Fluo-4. Duration of  $\text{Ca}^{2+}$  transients is higher after DA compared to that of spontaneous  $\text{Ca}^{2+}$  activity (basal). In  $\text{OCT3}^{-/-}$  astrocytes, the latency to  $\text{Ca}^{2+}$  recruitment in response to DA is similar to that observed in wild-type mice (see Fig. 3D). Data shown as slice averages (lines or transparent dots) and corresponding means  $\pm$  sem (solid dots and error bars). Duration (s):  $17 \pm 2$  (Baseline);  $53 \pm 10$  (DA). Peak latency:  $106 \pm 8$  s. Paired t-test after Anderson-Darling test; \*\*,  $p = 0.009$ ;  $n = 138$  active cells, 6 slices, 3 mice.

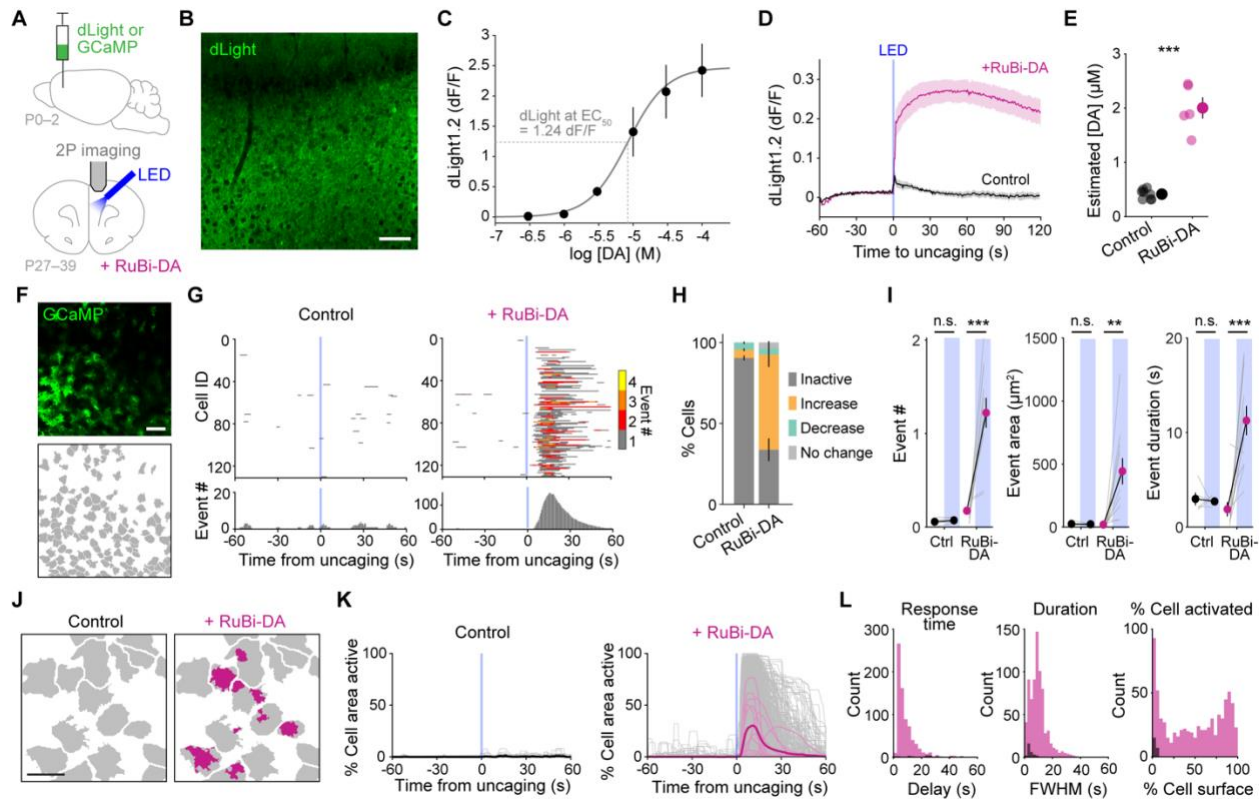


**Figure 4: Photo-uncaging in PFC releases physiological concentrations of DA and activates astrocyte territories within seconds.** (A) Experimental strategy for fast release of DA in PFC slices using RuBi-DA uncaging with a blue LED, combined with simultaneous 2P imaging of DA (dLight1.2) or astrocytic  $\text{Ca}^{2+}$  (GCaMP6f). (B) Representative dLight expression with 2P imaging in an acute PFC slice. Scale bar = 100  $\mu\text{m}$ . (C) Dose-response curve of dLight in PFC slices challenged with increasing concentrations of DA, and Hill equation fit function (solid line). Dotted lines indicate DA concentration at dLight half-maximum. Data shown as slice means  $\pm$  sem (dots and error bars);  $n = 4$  slices, 2 mice. (D) dLight fluorescence (dF/F) increases after LED stimulation (3x 100-ms pulses, blue line) in presence of the caged compound RuBi-DA (magenta) but not in the control without RuBi-DA in the bath (grey). Trace mean  $\pm$  sem;  $n = 6-7$  slices, 3 mice. (E) Estimated DA concentration after RuBi-DA uncaging was 2  $\mu\text{M}$ , extrapolated from fit function in (C) using data from (D) obtained as 30-s dF/F means after LED stimulation. Data shown as all slices (transparent dots) and corresponding mean  $\pm$  sem (solid dot and error bar):  $0.41 \pm 0.03$  (Control),  $2.0 \pm 0.2$  (RuBi-DA)  $\mu\text{M}$ . Two-sample t-test, \*\*\*,  $p < 10^{-6}$ ;  $n = 6-7$  slices, 3 mice. (F) Representative PFC slice expressing astrocytic GCaMP during 2P  $\text{Ca}^{2+}$  imaging (top) with corresponding cell maps drawn as boundaries around territories of individual astrocytes (bottom). Scale bar = 100  $\mu\text{m}$ . (G) Raster-plots of AQUA-detected  $\text{Ca}^{2+}$  events (top) show the time course of events within individual cells from slice in (F), plotted relative to LED stimulation (blue lines,  $t = 0$ ) before (left, control) and after bathing on RuBi-DA (right). Colors indicate co-occurring event number in each cell. Cumulative event counts across cells shown in bottom graphs. (H) Astrocyte  $\text{Ca}^{2+}$  activity increases for the majority of cells in the 60 s following RuBi-DA uncaging (70%), while cells are largely inactive (no  $\text{Ca}^{2+}$  events throughout the recording; 91%) in the control condition. Percentage of cells decreasing or maintaining (no change) their activity after uncaging is similar between conditions, indicating that DA does not induce a decrease in activity in a subset of astrocytes. Data shown as mean  $\pm$  sem;  $n = 540-1118$  cells, 5-11 slices, 5-8 mice. % Cells (Control, RuBi-DA):  $91 \pm 2$ ,  $30 \pm 7$  (Inactive);  $4 \pm 1$ ,  $62 \pm 8$  (Increase);  $4 \pm 1$ ,  $4 \pm 1$  (Decrease);  $0 \pm 0$ ,  $4 \pm 1$  (No change). (I)  $\text{Ca}^{2+}$  event features (number, area, duration) in active cells in (H) increase significantly in the 60 s after uncaging light (shaded blue boxes) with RuBi-DA (magenta) but not without (control, black). Slice averages of active cells (grey lines) and mean  $\pm$  sem

(dots and error bars). Event # (pre-, post-uncaging):  $0.06 \pm 0.02$ ,  $0.07 \pm 0.01$  (Control);  $0.17 \pm 0.03$ ,  $1.22 \pm 0.16$  (RuBi-DA). Event area ( $\mu\text{m}^2$ ):  $25 \pm 7$ ,  $23 \pm 3$  (Control);  $20 \pm 5$ ,  $443 \pm 104$  (RuBi-DA). Event duration (s):  $3.0 \pm 0.7$ ,  $2.7 \pm 0.2$  (Control);  $1.9 \pm 0.8$ ,  $11.3 \pm 1.5$  (RuBi-DA). Paired t-test comparing pre- to post-uncaging; \*\*,  $p < 0.01$ ; \*\*\*,  $p < 0.001$ . Control:  $n = 47/540$  active/total cells, 5 slices and mice. RuBi-DA:  $n = 784/1118$  cells, 11 slices, 8 mice. **(J)** Example of  $\text{Ca}^{2+}$  activation within individual cells 5 s after the uncaging pulse, either in control (left) or after addition of RuBi-DA (right). Maps are zoomed in from maps in (F). Grey = cell areas; magenta = active pixels. Scale bar = 50  $\mu\text{m}$ . **(K)** Time course of % cell area active relative to uncaging (blue lines) in absence (control) and presence of RuBi-DA. Data shown as cells, slices, and overall mean (grey, thin and thick colored lines, respectively). Control:  $n = 47/540$  cells, 5 slices and mice. RuBi-DA:  $n = 784/1118$  cells, 11 slices, 8 mice. **(L)** Astrocytic response to DA release (magenta) occurs within seconds of LED stimulation (left, delay), lasts  $< 20$  s (middle, peak full-width half-maximum), and recruits a wide range of areas within individual astrocytes (right, % cell surface). In controls (black), few cells were active after uncaging, with short activity ( $< 9$  s) covering a small percentage of cell area. Control:  $n = 22$  cells, 5 slices, 5 mice. RuBi-DA:  $n = 720$  cells, 11 slices, 8 mice.

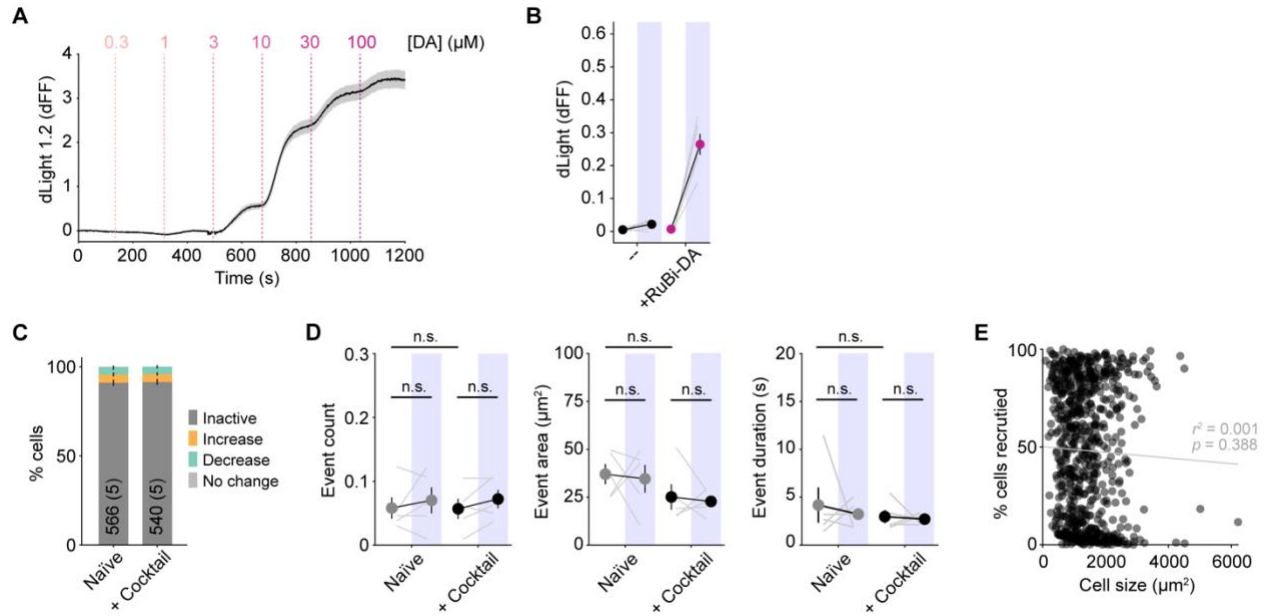


**Figure S4, related to Fig. 4.** (A) Representative dLight dose-response experiment, showing time course of dLight fluorescence in slices challenged with increasing concentrations of DA (0.3 to 100  $\mu\text{M}$ , in 1-log steps; times of application indicated by dotted lines and corresponding concentrations shown on top). Data shown as mean  $\pm$  sem of different regions-of-interest selected across the imaging field. (B) dLight1.2 fluorescence before and after uncaging (across 30s, shaded blue boxes) in PFC slices, in absence (-, black dots) or presence of RuBi-DA (magenta). Data from Fig. 4D, shown as slices (grey lines) and corresponding mean  $\pm$  sem (black lines, solid dots and error bars):  $0.005 \pm 0.002$ ,  $0.022 \pm 0.005$  (-);  $0.007 \pm 0.001$ ,  $0.265 \pm 0.032$  (+RuBi-DA). (C) Astrocytes were largely inactive (no  $\text{Ca}^{2+}$  events) before (naïve) and after addition of TTX and the multidrug cocktail (+ cocktail) used in all experiments in Fig. 4F–L. Percentage of cells increasing, maintaining, or decreasing their activity after the uncaging light pulse were low and similar between conditions, indicating no effect of light stimulation or drugs. Data shown as mean  $\pm$  sem;  $n = 540$ – $566$  cells, 5 slices, 5 mice. (D)  $\text{Ca}^{2+}$  event features (number, area and duration) in active cells in (C) were unchanged after addition of TTX and multidrug cocktail. There was similarly no effect of the uncaging light (shaded blue boxes) on event features in naïve slices and those treated with the cocktail. Data shown as slice means (grey lines) and mean  $\pm$  sem (dots and error bars). After checking normality, the Wilcoxon rank sum test was used to compare event features before uncaging between naïve and cocktail, and the paired t-test used to compare event features pre- versus post-uncaging. Naïve:  $n = 52/566$  cells, 5 slices and mice. Cocktail:  $n = 47/540$  cells, 5 slices, 5 mice. (E) The maximum cell area recruited by fast release of DA is independent of cell size, indicating that our cell delineation method does not affect this measurement.  $R^2$ , Pearson’s coefficient, and  $p$ ,  $p$ -value of linear correlation fit (grey line).  $N = 1118$  cells, 11 slices, 8 mice.

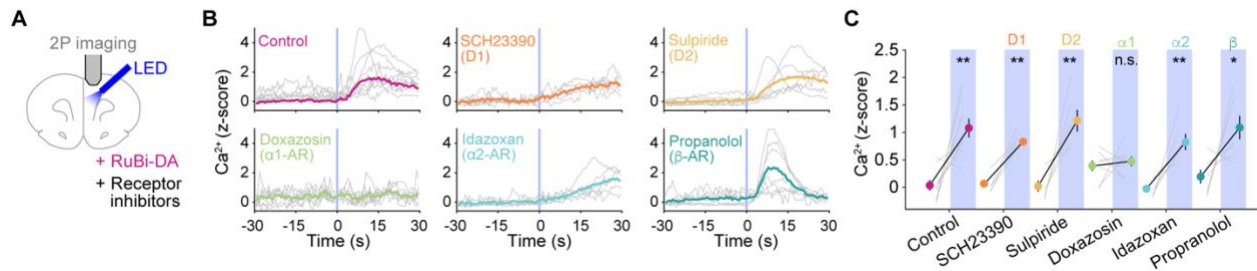


**Figure 5: Fast astrocyte responses to DA in PFC slices occur via  $\alpha 1$ -ARs.** (A) Experimental schematic for RuBi-DA uncaging and simultaneous 2P imaging of astrocyte  $\text{Ca}^{2+}$  in PFC slices bathed with different receptor antagonists. (B) Astrocyte  $\text{Ca}^{2+}$  in PFC slices increases shortly after RuBi-DA uncaging (control), an effect blocked by  $\alpha 1$ -AR antagonist Doxazosin (10  $\mu\text{M}$ ), but not by D1 (SCH23390, 10  $\mu\text{M}$ ), D2 (Sulpiride, 0.5  $\mu\text{M}$ ),  $\alpha 2$ -AR (Idazoxan, 10  $\mu\text{M}$ ) or  $\beta$ -AR (Propranolol, 10  $\mu\text{M}$ ) antagonists. Data relative to uncaging (blue lines,  $t = 0$ ) as slice average traces (grey lines) of AQuA-detected, z-scored  $\text{Ca}^{2+}$  events in GCaMP6f-expressing astrocytes, with overall mean as colored traces. (C) Quantification of (B), shown as 30-s mean of slice  $\text{Ca}^{2+}$  immediately before (white) or after RuBi-DA uncaging (shaded blue boxes) in presence of receptor inhibitors as indicated by labels. Data shown as slices (grey lines) and corresponding mean  $\pm$  sem (black lines, solid dots, and error bars):  $0.03 \pm 0.10$ ,  $1.08 \pm 0.17$  (control);  $0.07 \pm 0.07$ ,  $0.83 \pm 0.06$  (D1);  $0.02 \pm 0.10$ ,  $1.21 \pm 0.20$  (D2);  $0.39 \pm 0.10$ ,  $0.47 \pm 0.09$  ( $\alpha 1$ );  $-0.03 \pm 0.06$ ,  $0.82 \pm 0.15$  ( $\alpha 2$ );  $0.19 \pm 0.12$ ,  $1.09 \pm 0.21$  ( $\beta$ ). Paired t-test after Anderson-Darling test to compare pre- to post-uncaging values; \*,  $p < 0.05$ , \*\*,  $p < 0.01$ ;  $p = 0.004$  (control), 0.0006 (D1), 0.008 (D2), 0.624 ( $\alpha 1$ ), 0.008 ( $\alpha 2$ ), 0.036 ( $\beta$ );  $n = 6-9$  slices, 5-9 mice. Pre-uncaging values in treatments versus control were not statistically different (Kruskal-Wallis test with Dunn’s correction: adjusted p-value  $> 0.19$  for all comparisons).

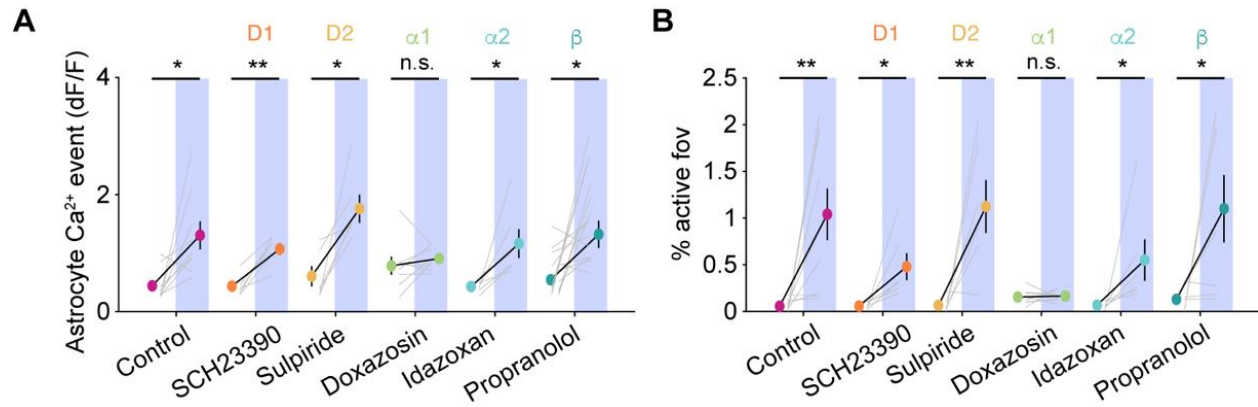


**Figure S5, related to Fig. 5.** (A–B) Additional quantification of experiments in Fig. 5B yield comparable results to z-scored traces of AQuA  $\text{Ca}^{2+}$ -events (Fig. 5C). (A) dF/F traces of AQuA  $\text{Ca}^{2+}$ -events. (B) Percent of active imaging field recruited over time. Data shown as 30-s means of slice  $\text{Ca}^{2+}$  immediately before or after RuBi-DA uncaging (shaded blue boxes) in presence of different receptor inhibitors as indicated, for slice averages (grey lines) and corresponding mean  $\pm$  sem (black lines, solid dots and error bars). One or two-tailed paired t-test or Wilcoxon signed rank test after checking normality with the Anderson-Darling test to compare pre- to post-uncaging values; \*,  $p < 0.05$ , \*\*,  $p < 0.01$ ;  $n = 6$ – $9$  slices, 5–9 mice.

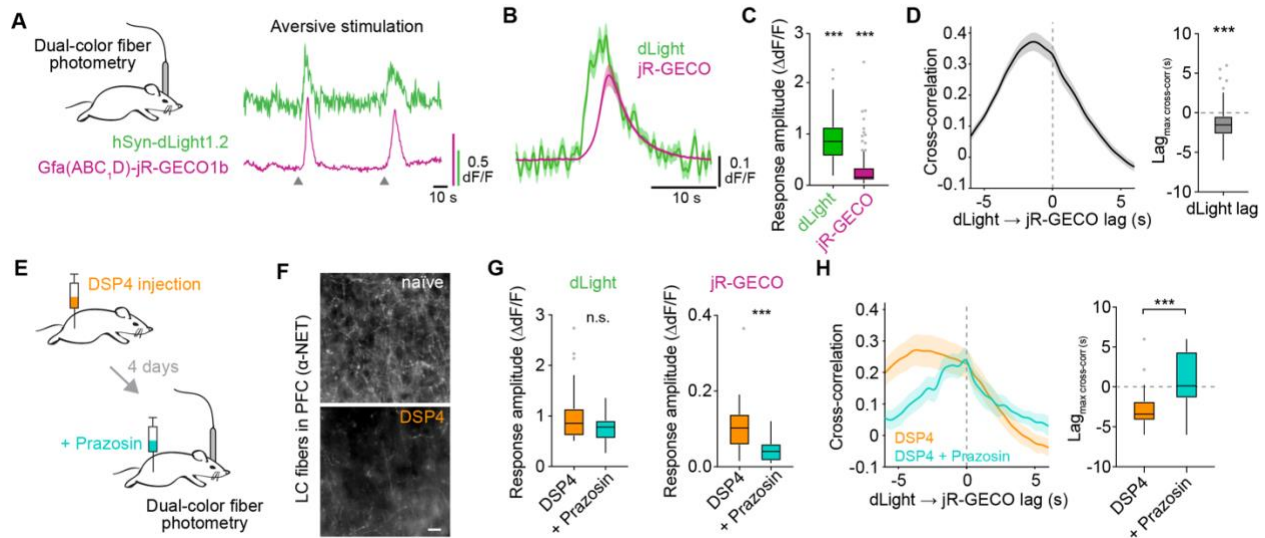


**Figure 6: Astrocyte Ca<sup>2+</sup> follows DA release *in vivo* via α1-ARs.** (A) Left: experimental setup for dual-color fiber photometry in PFC of behaving mice for recording DA (*hSyn*-dLight1.2, green) and astrocyte Ca<sup>2+</sup> (*GfaABC<sub>1</sub>D*-jR-GECO1b, magenta) dynamics. Right: example traces during aversive stimulation by tail lift (gray triangles). (B) Average photometry traces for DA and astrocyte Ca<sup>2+</sup> in PFC *in vivo*, aligned to the onset of astrocyte Ca<sup>2+</sup> transients. Data shown as mean ± sem; n = 96 transients, 9 mice. (C) Response amplitude for DA (green) and astrocyte Ca<sup>2+</sup> (magenta) in aversive stimulation experiments deviate significantly from baseline values (dLight: 0.89±0.04 dF/F; jR-GECO: 0.31±0.04 dF/F). Data shown as Tukey boxplots, calculated as maximum dF/F relative to 20-s mean before the jR-GECO peak. One-sample t-test or sign test with hypothesized mean 0, after Anderson-Darling test to show difference from 0; \*\*\*,  $p < 0.001$ ; n = 96 transients, 9 mice. (D) Cross-correlation of dLight and jR-GECO traces (left) indicates that DA signals in PFC *in vivo* precede astrocyte Ca<sup>2+</sup> transients by 1.4±0.2 s (right). Data shown as mean ± sem and Tukey boxplots; one-sample sign test with hypothesized mean 0, \*\*\*,  $p < 0.001$ ; n = 96 transients, 9 mice. (E) Schematic of dual-color fiber photometry in PFC of mice treated with the LC-toxin DSP4 (50 mg/kg, i.p., 2 injections, 2 days apart), before and after administration of the α1-AR antagonist Prazosin (5 mg/kg, i.p.). (F) LC inputs to PFC revealed by NET immunostaining (top, naïve) are decreased after DSP4 treatment (bottom). Scale bar = 50 μm. (G) In NE-depleted animals, DA transients (left, dLight) during aversive stimulation in PFC are still present (DSP4, orange; 1.02±0.11 dF/F) and unaffected when α1-ARs are blocked (+Prazosin, aqua; 0.77±0.05), whereas Ca<sup>2+</sup> peaks in astrocytes (right, jR-GECO) are significantly reduced by Prazosin treatment (DSP4: 0.11±0.01 dF/F; +Prazosin: 0.04±0.0 dF/F), indicating that astrocyte Ca<sup>2+</sup> in the PFC rely on α1-ARs even with diminished NE release. Data shown as Tukey boxplots, calculated as maximum dF/F relative to 20-s means before jR-GECO peaks. Wilcoxon rank sum test; \*\*\*,  $p = 0.0003$ ; n = 27–29 transients, 4 mice. (H) Cross-correlation of dLight and jR-GECO traces (left) in NE-depleted animals (DSP4), and in the same animals after inhibition of α1-ARs (DSP4 + Prazosin) shows that DA signals in PFC precede astrocyte Ca<sup>2+</sup> with diminished NE (DSP4, -2.64±0.52 s) but not after inhibition of α1-ARs (+Prazosin, 0.73±0.65 s). Data shown as trace mean ± sem and Tukey boxplots; Wilcoxon rank sum test; \*\*\*,  $p = 0.0003$ ; n = 27–29 transients, 4 mice.

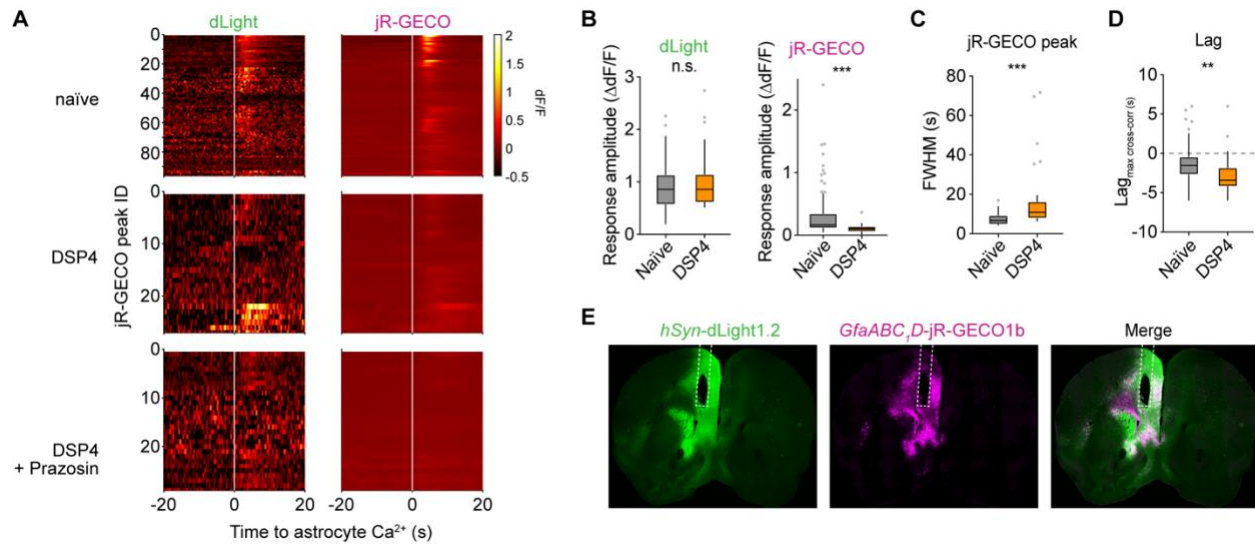


**Figure S6: Related to Fig. 6.** (A) Fiber photometry recordings of dLight (left) and astrocytic jR-GECO (right) aligned to the onset of astrocyte  $\text{Ca}^{2+}$  transients evoked by aversive stimulation ( $t = 0$ ), shown as heat map of  $\Delta\text{F}/\text{F}$  for all jR-GECO peaks detected and conditions (top: naïve; middle: DSP4; bottom: DSP4 and Prazosin). (B) Amplitude of DA transients (left, dLight) in PFC (naïve:  $0.89 \pm 0.04$   $\Delta\text{F}/\text{F}$ ) was not significantly affected by ablation of LC fibers (DSP4:  $1.02 \pm 0.11$   $\Delta\text{F}/\text{F}$ ), whereas astrocyte  $\text{Ca}^{2+}$  transients (right, jR-GECO) were significantly lower with decreased NE input (naïve:  $0.31 \pm 0.04$   $\Delta\text{F}/\text{F}$ ; DSP4:  $0.11 \pm 0.01$   $\Delta\text{F}/\text{F}$ ), indicating that the integrity of the NE system is important for astrocyte function in PFC. Data shown as Tukey boxplots. Wilcoxon rank sum test; \*\*\*,  $p < 0.001$ ;  $n = 27-96$  transients, 4–9 mice. (C) Astrocyte  $\text{Ca}^{2+}$  transients (jR-GECO peaks) were longer after decreased LC input to the PFC (naïve:  $7.3 \pm 0.3$  s; DSP4:  $18.3 \pm 3.5$  s). Data shown as Tukey boxplots. Wilcoxon rank sum test; \*\*\*,  $p < 0.001$ ;  $n = 27-96$  transients, 4–9 mice. (D) Lag of maximum cross-correlation between dLight and jR-GECO was significantly higher after decreased LC input to the PFC (naïve:  $-1.4 \pm 0.2$  s; DSP4:  $-2.6 \pm 0.5$  s). Data shown as Tukey boxplots. Wilcoxon rank sum test; \*\*,  $p = 0.004$ ;  $n = 27-96$  transients, 4–9 mice. (E) Optic fiber implant location in PFC was confirmed by immunostaining  $\sim 2$  mm rostral from Bregma to visualize expression of dLight (green) and jR-GECO1b in astrocytes (magenta), but note that implant location was determined initially by the stereotax coordinates.

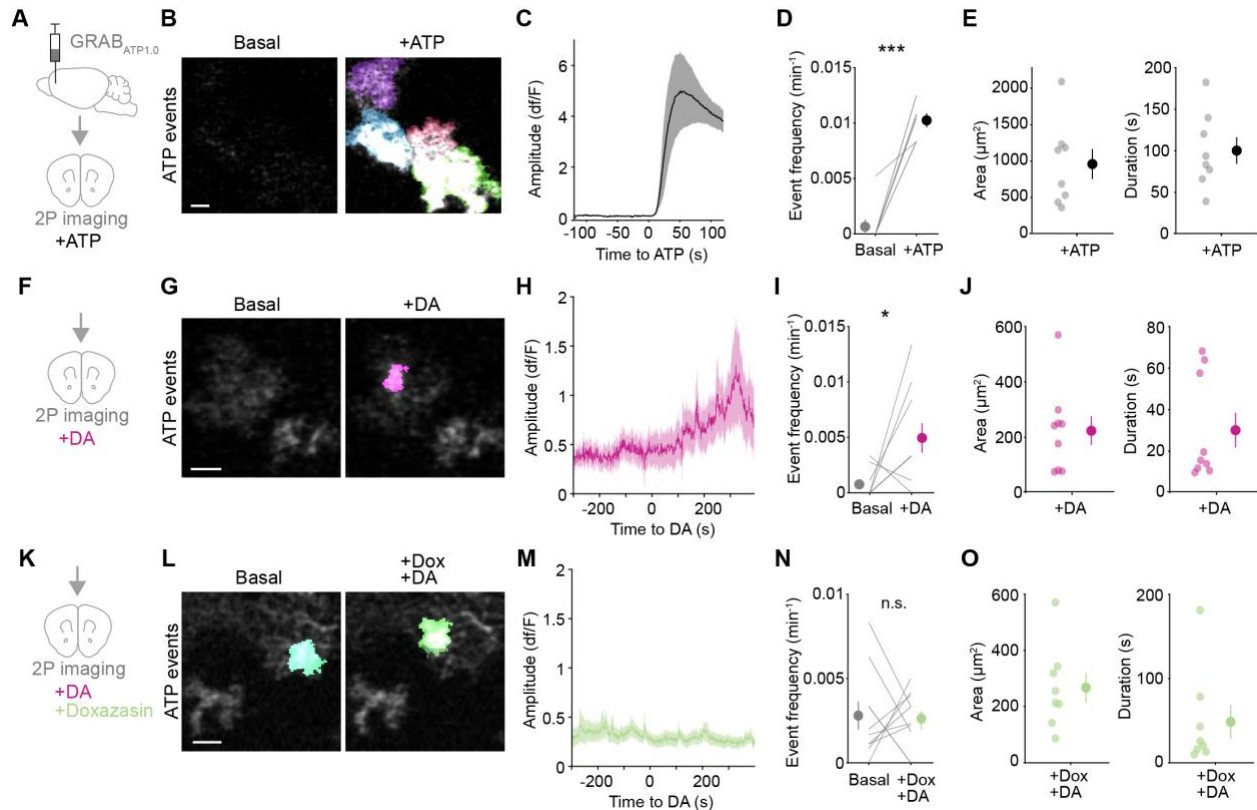


**Figure 7: DA mobilizes ATP at discrete locations at PFC astrocytes via  $\alpha_1$ -ARs.** (A) Experimental schematic for 2P astrocytic GRAB<sub>ATP</sub> imaging in acute PFC slices. (B–C) Continuous bath-application of ATP (50  $\mu$ M) induces strong, sustained fluorescent signals in astrocytes, shown as (B) PFC astrocytes expressing GRAB<sub>ATP</sub> (grayscale) and color overlay of AQuA-detected ATP events before (left, basal) and after ATP (right), and (C) time course of the dF/F amplitude of AQuA-detected ATP events relative to exogenous ATP application (t = 0). Scale bar = 20  $\mu$ m. Data shown as mean  $\pm$  sem of slice traces (line and shaded area). n = 52/62 active/total cells, 8 slices, 3 mice. (D) GRAB<sub>ATP</sub> event rate increases following stimulation with ATP. Data shown as slice averages (lines) and mean  $\pm$  sem (dots and error bars):  $0.0007 \pm 0.0007$  (Basal),  $0.010 \pm 0.001$  (+ATP) min<sup>-1</sup>. Paired t-test after Anderson-Darling test; \*\*\*,  $p < 10^{-4}$ ; n = 8 slices, 3 mice. (E) GRAB<sub>ATP</sub> events in response to continuous ATP application covered the entire sensor-expressing astrocyte territory (left,  $1044 \pm 224$   $\mu$ m<sup>2</sup>) and were sustained (right,  $100 \pm 16$  s) as expected. Data shown as slice averages of active cells (transparent dots) and overall mean  $\pm$  sem (solid dots and error bars); n = 8 slices, 3 mice. (F–H) Application of DA (10  $\mu$ M) onto PFC astrocytes expressing GRAB<sub>ATP</sub> (F) induces localized ATP events, shown as (G) GRAB<sub>ATP</sub> micrographs and AQuA overlay, which are delayed (H) as shown by the time course of GRAB<sub>ATP</sub> event dF/F relative to DA application (t = 0). Scale bar = 20  $\mu$ m. Data shown as mean  $\pm$  sem of slice averages (line and shaded area). n = 23/101 active/total cells, 10 slices, 5 mice. (I) Rate of ATP events after DA application was higher than baseline. Data shown as slice averages (lines) and mean  $\pm$  sem (dots and error bars):  $0.0007 \pm 0.0004$  (Basal),  $0.005 \pm 0.001$  (+DA) min<sup>-1</sup>. Paired t-test after Anderson-Darling test; \*,  $p = 0.025$ ; n = 10 slices, 5 mice. (J) GRAB<sub>ATP</sub> events in response to DA were smaller than entire astrocyte territories ( $221 \pm 52$   $\mu$ m<sup>2</sup>) and time-restricted ( $30 \pm 8$  s). Data shown as slice averages of active cells (transparent dots) and overall mean  $\pm$  sem (solid dots and error bars); n = 9 slices, 5 mice. (K–M) In presence of the  $\alpha_1$ -AR antagonist Doxazosin (10  $\mu$ M), DA (K) does not induce ATP events, as shown by (L) GRAB<sub>ATP</sub> micrographs and AQuA overlay, and (M) time-course of GRAB<sub>ATP</sub> event dF/F relative to DA application (t = 0, 10  $\mu$ M). Scale bar = 20  $\mu$ m. Data shown as mean  $\pm$  sem of slice averages (line and shaded area). n = 41/160 active/total cells, 10 slices, 5 mice. (N) In presence of Doxazosin, DA application does not

increase the rate of ATP events. Data shown as slice averages (lines) and mean  $\pm$  sem (dots and error bars):  $0.0028 \pm 0.0008$  (Basal),  $0.0026 \pm 0.0005$  (+Dox/+DA)  $\text{min}^{-1}$ . Paired t-test after Anderson-Darling test; n.s.,  $p = 0.878$ ;  $n = 10$  slices, 5 mice. **(O)** GRAB<sub>ATP</sub> events in presence of Doxazosin are similar in size ( $267 \pm 53 \mu\text{m}^2$ ) and duration ( $48 \pm 20$  s) compared to those observed in response to DA alone. Data shown as slice averages of active cells (transparent dots) and overall mean  $\pm$  sem (solid dots and error bars);  $n = 10$  slices, 5 mice.

## Supplemental Movies

### **Movie 1: PFC astrocytes *in vivo* display cell-restricted Ca<sup>2+</sup> activity unlinked to animal locomotion.**

Ca<sup>2+</sup> events in PFC (left) and V1 (right) astrocytes, with their relationship to animal locomotion. Top: raw Lck-GCaMP6f movies with overlaid AQUA-detected Ca<sup>2+</sup> events (colors are individual events). Bottom: time course of astrocyte activity shown as population-level Ca<sup>2+</sup> traces with corresponding animal locomotion speed below. Images acquired at 2 Hz, playback speed 15 fps.

### **Movie 2: Robust astrocyte Ca<sup>2+</sup> response to DA stimulation of PFC slices.**

Bath-application of DA (10 μM) in PFC slices expressing GCaMP6f in astrocytes induces a robust, but delayed Ca<sup>2+</sup> mobilization. Neuronal action potentials and neuron-to-astrocyte communication are blocked with TTX and a drug cocktail (see Methods). Top: raw movie; bottom: AQUA-detected Ca<sup>2+</sup> events. Time stamps relative to DA application.

### **Movie 3: DA uncaging induces fast, transient Ca<sup>2+</sup> activation in PFC astrocytes.**

RuBi-DA (right) uncaged at t=0 on GCaMP6f-expressing astrocytes in a PFC slice, inducing a robust Ca<sup>2+</sup> response within seconds. In the same slice, the light stimulation protocol in the absence of RuBi-DA (control, left) has no effect. Top: raw movies; bottom: overlaid AQUA-detected Ca<sup>2+</sup> events (colors are individual events). Time indicated in seconds from uncaging.

### **Movie 4: DA acts on PFC astrocytes via α1-adrenergic receptors.**

Representative experiments in PFC slices expressing GCaMP6f in astrocytes, in which RuBi-DA is uncaged at t = 0 s in presence of different DR and AR antagonists. Labels indicate drugs (Control: no antagonist; D1: SCH23390 10 μM; D2: Sulpiride 0.5 μM; α1: Doxazosin 10 μM; α2: Idazoxan 10 μM; β: Propranolol 10 μM). Uncaging light pulses appear as white stripes due to detector saturation. Only Doxazosin application blocks uncaging-induced astrocyte activation.

## Methods

### Animals

Experiments were carried out using young adult for *ex vivo* or adult mice for *in vivo* experiments, in accordance with protocols approved by the University of California, San Francisco Institutional Animal Care and Use Committee (IACUC). Animals were housed in a 12:12 light-dark cycle with food and water provided *ad libitum*. Male and female mice were used whenever available. For *in vivo* experiments following surgery, all animals were singly housed to protect implants and given additional enrichment. Transgenic mice used in this study were Lck-GCaMP6f<sup>fl/fl</sup> mice (Srinivasan et al., 2016) and *Aldh111*-Cre/ERT2 mice (Srinivasan et al., 2016) from the Khakh lab (UCLA, USA), *Drd1a*-tdTomato (Shuen et al., 2008) and *Drd2*-EGFP (Gong et al., 2003) from the Bender lab (UCSF, USA), *Aldh111*-EGFP and *Aldh111*-tdTomato (Gong et al., 2003) from JAX (USA), *Itpr2*-deficient mice (IP<sub>3</sub>R2<sup>-/-</sup>) (Li et al., 2005) from Dr. Katsuhiko Mikoshiba (RIKEN, Japan) and *Slc22a3*-deficient mice (OCT3<sup>-/-</sup>) (Zwart et al., 2001) from the Irannejad lab (UCSF, USA).

### Surgical procedures

For viral expression in *ex vivo* experiments, neonatal mice (P0–4) on C57Bl/6 or Swiss background were anesthetized on ice for 2 min before injecting viral vectors (AAV5-*GfaABC1D-GCaMP6f* [1.4–5.42e<sup>13</sup>; all titers in GC/ml], AAV9-*hGfap-pinkFlamindo* [6.6e<sup>13</sup>], AAV9-*hSyn-NE2.1* [5.72e<sup>13</sup>], AAV9-*CAG-dLight1.2* [9.5e<sup>15</sup>], or AAV9-*hSyn-ATP1.0* [4.89e<sup>13</sup>]). Pups were placed on a digital stereotax and coordinates were zeroed at the middle point along the line connecting the eyeballs. Two injection sites over PFC were chosen at 0.25–0.34 mm lateral, and 1 and 1.4 mm caudal. At each injection site, 30–100nl of virus were injected at a rate of 3–5nl/s at two depths (0.7–0.85, and 0.9–1 mm ventral) using a microsyringe pump (UMP-3, World Precision Instruments).

For *in vivo* 2P imaging, we expressed Lck-GCaMP in astrocytes of adult mice (P50–130), either by crossing Lck-GCaMP6f<sup>fl/fl</sup> mice to *Aldh111*-Cre/ERT2 (Srinivasan et al., 2016) and treating them with tamoxifen (0.1 mg/kg, i.p., for 5 consecutive days, 4–6 weeks before imaging), or via viral vectors (see below) in C57Bl/6 mice. For fiber photometry, we expressed dLight and astrocytic jR-GECO1b via viral vectors (see below) in C57Bl/6 mice (P60–90). Before surgical procedures, adult mice were administered dexamethasone (5 mg/kg, s.c.) and anesthetized with isoflurane, and a 1 or 3-mm diameter craniotomy was created over PFC (+1.7–1.8 mm rostral, +0.5 mm lateral from Bregma) or visual cortex (-3.5 mm caudal, +1.2 mm lateral from Bregma). Viral vectors (AAV5-*GfaABC1D-Lck-GCaMP6f-SV40* [1.4–5.42e<sup>13</sup>], AAV5-*hSyn-dLight1.2* [4e<sup>12</sup>], AAV9-*GfaABC1D-Lck-jRGECO1b* [2.24e<sup>14</sup>]) were delivered using a microsyringe pump (100–600 nl, 30–60 nl/min) before implanting optical devices. For 2P imaging in PFC, after careful removal of meninges, a GRIN lens (1-mm diameter, 4.38-mm length, WDA 100, 860

nm, Inscopix) was slowly lowered to -2.4 mm ventral; for 2P imaging in V1, a cranial window was placed above the tissue; a custom-made titanium headplate was then attached to the skull. For fiber photometry in PFC, a fiber optic cannula (Mono Fiberoptic Cannula, 400 $\mu$ m core, 430nm, 0.48 NA, 2.8mm length, Doric Lenses) was implanted at the same depth as GRIN lenses. All imaging devices were secured in place using dental cement (C&B Metabond, Parkell). Post-operative care included administration of 0.05 mg/kg buprenorphine and 5 mg/kg carprofen. Mice were allowed a minimum of 14 days to recover, then habituated to head-fixation on a circular treadmill or to fiber optic coupling in a freely moving arena prior to experiments.

#### *In vivo 2P imaging and locomotion*

2P imaging experiments were carried out on an upright microscope (Bruker Ultima IV) equipped with a Ti:Sa laser (MaiTai, SpectraPhysics). The laser beam intensity was modulated using a Pockels cell (Conoptics) and scanned with linear galvanometers. Images were acquired with a 16 $\times$ , 0.8 N.A. (Nikon) or a 20 $\times$ , 1.0 N.A. (XLUMPLFLN-W, Olympus) water-immersion objective via photomultiplier tubes (Hamamatsu) using PrairieView (Bruker) software. For GCaMP imaging, 950 nm excitation and a 515/30 emission filter were used. Mice were head-fixed on a circular treadmill and Ca<sup>2+</sup> activity was recorded at ~1.7 Hz frame rate from putative PFC or V1 cortex, at 512 $\times$ 512 pixels and ~0.6  $\mu$ m/px resolution. Locomotion speed was monitored using an optoswitch (50mA, 2V; OPB800L55, TT Electronics, Newark) connected to a microcontroller board (Arduino Uno R3, Arduino) and acquired at 1KHz simultaneously with 2P imaging using PrairieView.

#### *Ex vivo 2P imaging and uncaging*

Coronal, acute PFC slices (300- $\mu$ m thick) from P27–P54 mice were cut with a vibratome (VT 1200, Leica) in ice-cold cutting solution containing (in mM) 27 NaHCO<sub>3</sub>, 1.5 NaH<sub>2</sub>PO<sub>4</sub>, 222 sucrose, 2.6 KCl, 2 MgSO<sub>4</sub>, 2 CaCl<sub>2</sub>. Slices were transferred to pre-heated, continuously aerated (95% O<sub>2</sub>/5% CO<sub>2</sub>) standard artificial cerebrospinal fluid (ACSF) containing (in mM) 123 NaCl, 26 NaHCO<sub>3</sub>, 1 NaH<sub>2</sub>PO<sub>4</sub>, 10 dextrose, 3 KCl, 2 MgSO<sub>4</sub>, 2 CaCl<sub>2</sub>. Younger mice were sliced in the same solutions for dLight (P18–28) and GRAB<sub>NE</sub> (P24–35) experiments, and one P19 IP<sub>3</sub>R2<sup>-/-</sup> experiment (otherwise P31–36). Slices were kept at room temperature until imaging, and experiments performed at 37°C. To block neuronal action potentials and neuron-to-astrocyte-communication during imaging, at least 10 min before experiments recirculating standard ACSF was switched to a multi-drug cocktail mix, containing (in  $\mu$ M) 1 TTX, 100 LY341495, 1 CGP 55845, 2 AM251, 1 CGS 15943, 100 PPADS, 5 Ipratropium, unless otherwise stated.

Slice recordings were done in coronal sections above medial prefrontal cortex, and the imaging area was ~ 0.6–0.8 mm x 0.8 mm over prelimbic and infralimbic areas, with the top part of the imaging area corresponding to the midline, thus spanning all cortical layers. Images were acquired from putative PL-IL

cortex in PFC slices at a minimum depth of 50  $\mu\text{m}$ , using the same setup as for *in vivo* 2P imaging or a custom-made upright microscope and ScanImage software, at 1.42–1.53 Hz frame rate, 512 $\times$ 512 pixels and 1.04–1.61  $\mu\text{m}/\text{px}$  resolution. Fluorophores were excited at (in nm) 950–980 (GCaMP), 1040 (Pink Flamindo), 980 (dLight), 920 (GRAB<sub>NE</sub> and GRAB<sub>ATP</sub>). Emission was collected with a 515/30 or 525/50 filter for green and a 605/15 or 600/40 filter for red fluorophores. For bath-application experiments, a 5-min baseline was recorded to monitor spontaneous activity, after which neuromodulators were added along with a fluorescent dye (AlexaFluor 594 Hydrazide) to assess the time at which drugs reached the imaging field (except for Pink Flamindo due to spectral overlap).

For RuBi-DA uncaging, a fiber optic cannula (400- $\mu\text{m}$  core, 0.39 NA; CFM14L10, ThorLabs) was coupled to a compatible fiber optic (M79L005, ThorLabs) and a blue LED (470 nm; M470F3, ThorLabs), and placed adjacent to the imaging field using a micromanipulator (MX160R, Siskiyou). Illumination (3 pulses, 100-ms duration, 50-ms intervals) was triggered using the imaging software (PrairieView, Bruker) connected to the LED-driver cube (LEDD1B, ThorLabs). Light power was 2–4 mW.

#### *Fiber photometry recordings*

FP experiments were carried out using an RZ10 fiber photometry processor equipped with Lux integrated 405, 465, and 560-nm LEDs and photosensors (Tucker-Davis Technologies). Animals implanted for FP were placed in a freely moving arena in which the mouse was able to move in all directions, after coupling to low autofluorescence fiberoptic patchcords (400- $\mu\text{m}$  core, 0.57 NA; Doric Lenses) connected to photosensors through a rotary joint (Doric Lenses). FP fluorescence signals were recorded for 10 minutes, during which tail lifts were performed every minute. For a tail lift stimulation, the experimenter held and lifted the tail of the animal until its hind paws disconnected from the ground; after that the tail was released. With this experimental paradigm, no pain or harm is caused to the animal. After baseline recordings, animals were treated with DSP4 (50 mg/kg, i.p., 2 injections 2 days apart) and recorded again 4 days after the first DSP4 administration. Following DSP4 recordings, animals were injected with Prazosin (5 mg/kg, i.p.) and recorded again 20 minutes later.

#### *Immunohistochemistry*

Mice were intracardially perfused with 4% PFA, brains were then collected, immersed in 4% PFA overnight at 4°C and switched to 30% sucrose for two days before being frozen on dry ice and stored at -80°C. Brains were sliced coronally (40- $\mu\text{m}$  thick) on a cryostat, and slices stored in cryoprotectant at -20°C until staining. Slices were washed 3x in PBS for 5 min, then permeabilized for 30 min with 0.01% TritonX in PBS. Slices were next washed with 10% NGS (Invitrogen) for 1 h and incubated overnight with primary antibodies at 4°C in 2% NGS. Slices were next rinsed 3x in PBS before incubating for 2 h at

room temperature with secondary antibodies, then washed 3x in PBS for 5 min before slide-mounting and coverslipping using Fluoromount with DAPI.

To stain for EGFP and tdTomato in D1, D2 and Aldh1l1 colocalization experiments, primary antibodies used were rat  $\alpha$ -mCherry (1:1000, Thermo Fisher Scientific) and chicken  $\alpha$ -GFP (1:3000, Aves Lab) in 2% NGS. Secondary antibodies used were goat  $\alpha$ -rat Alexa Fluor 555 (1:1000) and goat  $\alpha$ -chicken Alexa Fluor 488 (1:1000). To estimate colocalization, 3 slices/mouse were chosen at +1.8, +1.7 and +1.6 mm from bregma, and tiled z-stack images were acquired on a spinning disk confocal (Zeiss) at PFC spanning cortical layers 1–6. Colocalization counts of tdTomato<sup>+</sup> and EGFP<sup>+</sup> cells were performed using Cell Counter in Fiji (ImageJ).

To stain brain tissue from GRIN lens experiments, primary antibodies used were rat  $\alpha$ -GFAP (1:1000, Thermo Fisher Scientific) and chicken  $\alpha$ -GFP (1:3000, Aves Lab) for Lck-GCaMP. To stain for dLight and jR-GECO1b in sections from fiber photometry experiments, primary antibodies used were rat  $\alpha$ -mCherry (1:1000, Thermo Fisher Scientific) and chicken  $\alpha$ -GFP (1:3000, Abcam). Secondary antibodies used were goat  $\alpha$ -rat Alexa Fluor 555 (1:1000, Thermo Fisher Scientific) and goat  $\alpha$ -chicken Alexa Fluor 488 (1:1000, Thermo Fisher Scientific). For NET staining, sections were incubated for 1 h with a secondary mouse block (AffiniPure Fab Fragment IgG, 30  $\mu$ g/ml, Jackson ImmunoResearch) before primary antibody mouse  $\alpha$ -NET (1:100, MAb Technologies), and secondary antibody goat  $\alpha$ -mouse Alexa Fluor 555 (1:1000, Thermo Fisher Scientific). Z-stacks or whole-brain images were acquired at 40x or 2x using a Keyence BZ-X800 fluorescence microscope and stitched with Keyence Analysis Software.

### *2P image and data analysis*

When necessary, videos were preprocessed by registering images using the ImageJ plugin MoCo (Dubbs et al., 2016). Cell maps for Pink Flamingo, GRAB<sub>ATP</sub>, and uncaging experiments were drawn using the interactive wand segmentation tool (SCF-MPI-CBG plugin).

**AQuA:** Ca<sup>2+</sup> and ATP 2P image sequences were analyzed using AQuA software (Wang et al., 2019) and custom MATLAB (Mathworks) code. Signal detection thresholds were adjusted for each video to account for differences in noise levels after manually checking for accurate AQuA-detection. Events were thresholded post-detection at 25  $\mu$ m<sup>2</sup> and 2 s for *ex vivo*, or 50  $\mu$ m<sup>2</sup> and 2 s for *in vivo* Ca<sup>2+</sup> imaging, and at 50  $\mu$ m<sup>2</sup> and 2.5 s for GRAB<sub>ATP</sub> imaging. Event count was quantified using the onset of each event as detected by AQuA. Area is defined as the footprint occupied by an event over its entire lifetime. Number of co-occurring events is calculated as the number of events co-existing temporally anywhere in the imaging field with a given event. Number of co-localized events is calculated as the number of events having comparable size (0.5–2x) and overlapping spatially with a given event.

**In vivo 2P Ca<sup>2+</sup> imaging and locomotion analysis:** For locomotion-aligned astrocyte Ca<sup>2+</sup> analysis, only locomotion bouts longer than 2 s and starting more than 10 s after the previous locomotion bout ended were considered (Fig S1H). Population-wide mean Ca<sup>2+</sup> traces (Fig 1I) were obtained by normalizing the fluorescence of each AQuA-detected event as  $(F - F_{\min}) / (F_{\max} - F_{\min})$  and then averaging across events. For max Ca<sup>2+</sup> (Fig 1K), changes in normalized fluorescence were thresholded at 0.1 to exclude noise. For astrocyte Ca<sup>2+</sup>-aligned locomotion analysis (Fig 1L), astrocyte Ca<sup>2+</sup> event dF/F was used and all locomotion bouts were considered. Locomotion speed was calculated as cm/s.

**Bath-applied DA analysis:** For bathed-DA experiments, Ca<sup>2+</sup> event rate was calculated as counts of AQuA-event onsets in 5-s bins (Ca<sup>2+</sup>), and events for the post-treatment condition (Fig 3E) were analyzed over a 30-s window centered at 90-s post drug or at the timepoint when the event rate exceeds baseline (6 STD of event rate at baseline). We then calculated the peak onset as the last local minimum before the peak, and—to overcome false positives due to noise—we constrained the local minima to be below the 6 STD threshold for peak detection. At baseline (Fig S3B) we used a 60-s window to account for low number of spontaneous events. For GRAB<sub>ATP</sub>, events were analyzed over 300-s windows, immediately before (basal) and 90-s post drug. The 300-s window (for the post-drug condition) was started 90-s after the delivery of the drug since we wanted to probe ATP events that would follow DA-induced Ca<sup>2+</sup> events, which—in bath application experiments (Fig. 3)—started ~90 s after drug delivery.

**Single-cell ex vivo uncaging analysis:** Classification of cell activity around uncaging was done based on counts of AQuA-event onsets in the 60-s before versus 60-s after uncaging (t=0). Event features (count, area, duration) were averaged by cell and slice using the same temporal windows. Traces for the % of cell area active were obtained as the overall number of pixels/frame occupied by AQuA-detected events within an individual astrocyte (cell territories were defined by cell maps, see above). Traces were analyzed with custom-written code in MATLAB to find peak times, amplitudes (max % cell surface active) and duration (FWHM). Latency to peak onset after uncaging (delay) was obtained as the first timepoint above threshold (6 STD of the pre-uncaging activity).

**ROI-based analysis:** Pink Flamingo, GRAB<sub>NE</sub> and dLight videos were analyzed using ROI-based approaches in ImageJ. Changes in fluorescence intensity were calculated as  $(F - F_0) / F_0$  (dF/F), where F<sub>0</sub> is the average intensity of the first 20–30 frames. For GRAB<sub>NE</sub>, dF/F values were extracted as 20-s means at 50 s before (pre-drug) or 340 s after compound addition. Fluo-4 videos from OCT3 KO experiments were analyzed using CalTracer 3 Beta (Poskanzer and Yuste, 2016), dF/F traces extracted from the automatically detected cell somata, and identified peaks checked manually for accurate detection before extracting duration and latency. Traces dF/Fs were then obtained as 5-s means at 100 s before or after DA addition based on average peak latencies. Data for the dLight dose-response curves were fit to a Hill equation ( $y = a + (b - a) / (1 + 10^{((c - x) * d)})$ ), and DA concentrations released by RuBi-DA uncaging were

extrapolated from the obtained fit function based on changes in dLight fluorescence after uncaging.

***Pink Flamindo analysis:*** For Pink Flamindo experiments, background fluorescence was subtracted from raw fluorescence traces. To identify steady-state increases or decreases in fluorescence, traces were smoothed using a moving average and then fit using a modified Boltzmann's sigmoidal equation  $y=a+(b-a)/(1+\exp((c-x)/d))$ , where  $a$  is the bottom,  $b$  is the top,  $c$  is the inflection point and  $d$  is the slope, using a nonlinear least squares algorithm (Levenberg-Marquardt) in MATLAB. Fit constraints were  $(b-a) > \text{noise}$ ,  $\text{slope} < 10$ , and inflection point at  $x > 0$ . Cells where the sigmoid fit of the trace in response to Forskolin did not converge were excluded from all previous analyses. Cells with high noise ( $>0.1$  dF/F) or drift (when change in dF/F before drug application exceeded noise) were removed. Noise was calculated as 3 STD at baseline. Average dF/F values (Fig 2G) were then extracted as 20-s means at 40 s before (control) or 240 s after compound addition (drug/Forskolin) from original traces.

#### *Fiber photometry analysis*

FP data were preprocessed by downsampling and subtraction of the isosbestic channel linear fit (as in <https://www.tdt.com/docs/sdk/offline-data-analysis/offline-data-python/FibPhoEpoCAveraging>), detrended to correct bleaching, and dF/F calculated as above ( $F_0$  obtained at 0–15 s). Traces were then denoised using an IIR lowpass filter in MATLAB (cutoff frequency 1Hz, steepness 0.95). Transients in jR-GECO1b traces were detected using the 'findpeaks' function in MATLAB (applied over normalized traces, with minimum peak height and prominence set to 25% and at a minimum distance of 20 s, according to the timing of the tail lift stimulation protocol. All trials/animals were analyzed using the same parameters for peak detection.) Transient onsets were determined as the timepoints where the first derivative exceeded 1 STD. Then, dLight and jR-GECO1b traces were extracted in 40-s windows centered at onsets, and the cross-correlation function calculated from the extracted traces with a 6-s maximum lag to obtain the latency to maximum cross-correlation. Response amplitudes (Fig 6C,G) were calculated for each detected peak as change in dF/F between trace average before onset and trace maximum after onset.

#### *Statistics*

To compare one group of data with a hypothesized mean value we used a one-sample t-test or sign test (Wilcoxon) as appropriate after a normality test. When comparing two unpaired groups, we used the two-sample, unpaired t-test or the Wilcoxon rank sum test (Mann-Whitney) as appropriate after a normality test. When comparing two paired groups of data, we used the paired t-test or the Wilcoxon signed rank test after checking for normality on the difference between groups. Normality was checked using the Anderson-Darling test. When comparing treatments for three or more groups (Fig 3E,G) we

used one-way Anova or the Kruskal-Wallis test after testing for equal variances using the Levene test (quadratic). For Pink Flamindo data (Fig 2G), we used the non-parametric Friedman test for paired data after the Levene test to compare within conditions (control, drug, Forskolin), and one-way Anova or Kruskal-Wallis test after the Levene test to compare across treatments. Multiple comparisons in Fig. 5 were not corrected *post hoc* to minimize type II errors (i.e., to avoid increasing the rate of false negatives; in a false negative, pre- to post-uncaging values would be erroneously considered non-significantly different from each other). All statistical tests are two-tailed unless otherwise stated in the figure legend (Fig. S5B).

Statistical significance for time-series data was computed using the shuffle test with custom-written code in MATLAB. Data pairs were selected as a reference value (trace mean from  $t < 0$  or the entire time window analyzed) and a given timepoint in the time-series ( $t > 0$  or all timepoints in the window). Data from the two groups were pair-wise shuffled for 10000 repetitions to calculate the difference between the two populations, the significance level  $\alpha$  for rejecting  $H_0$  was set to 0.01, and Bonferroni correction was applied to account for multiple comparisons.

## Bibliography

- Abbink, M.R., van Deijk, A.-L.F., Heine, V.M., Verheijen, M.H., and Korosi, A. (2019). The involvement of astrocytes in early-life adversity induced programming of the brain. *Glia* 67, 1637–1653.
- Abercrombie, E.D., Keefe, K.A., DiFrischia, D.S., and Zigmond, M.J. (1989). Differential effect of stress on in vivo dopamine release in striatum, nucleus accumbens, and medial frontal cortex. *J. Neurochem.* 52, 1655–1658.
- Agnati, L.F., Zoli, M., Strömberg, I., and Fuxe, K. (1995). Intercellular communication in the brain: wiring versus volume transmission. *Neuroscience* 69, 711–726.
- Alachkar, A., Brotchie, J.M., and Jones, O.T. (2010). Binding of dopamine and 3-methoxytyramine as 1-DOPA metabolites to human alpha(2)-adrenergic and dopaminergic receptors. *Neurosci. Res.* 67, 245–249.
- Amphoux, A., Vialou, V., Drescher, E., Brüß, M., Mannoury La Cour, C., Rochat, C., Millan, M.J., Giros, B., Bönisch, H., and Gautron, S. (2006). Differential pharmacological in vitro properties of organic cation transporters and regional distribution in rat brain. *Neuropharmacology* 50, 941–952.
- Anastasiades, P.G., Boada, C., and Carter, A.G. (2019). Cell-Type-Specific D1 Dopamine Receptor Modulation of Projection Neurons and Interneurons in the Prefrontal Cortex. *Cereb. Cortex* 29, 3224–3242.
- Araya, R., Andino-Pavlovsky, V., Yuste, R., and Etchenique, R. (2013). Two-photon optical interrogation of individual dendritic spines with caged dopamine. *ACS Chem. Neurosci.* 4, 1163–1167.
- Arnsten, A.F.T., Wang, M.J., and Paspalas, C.D. (2012). Neuromodulation of thought: flexibilities and vulnerabilities in prefrontal cortical network synapses. *Neuron* 76, 223–239.
- Azdad, K., Gall, D., Woods, A.S., Ledent, C., Ferré, S., and Schiffmann, S.N. (2009). Dopamine D2 and adenosine A2A receptors regulate NMDA-mediated excitation in accumbens neurons through A2A-D2 receptor heteromerization. *Neuropsychopharmacology* 34, 972–986.
- Banasr, M., and Duman, R.S. (2008). Glial loss in the prefrontal cortex is sufficient to induce depressive-like behaviors. *Biol. Psychiatry* 64, 863–870.
- Banerjee, A., Lee, J., Nemcova, P., Liu, C., and Kaeser, P.S. (2020). Synaptotagmin-1 is the Ca<sup>2+</sup> sensor for fast striatal dopamine release. *Elife* 9.
- Barbosa, J., Stein, H., Martinez, R.L., Galan-Gadea, A., Li, S., Dalmau, J., Adam, K.C.S., Valls-Solé, J., Constantinidis, C., and Compte, A. (2020). Interplay between persistent activity and activity-silent dynamics in the prefrontal cortex underlies serial biases in working memory. *Nat. Neurosci.* 23, 1016–1024.

- Batiuk, M.Y., Martirosyan, A., Wahis, J., de Vin, F., Marneffe, C., Kusserow, C., Koeppen, J., Viana, J.F., Oliveira, J.F., Voet, T., et al. (2020). Identification of region-specific astrocyte subtypes at single cell resolution. *Nat. Commun.* *11*, 1220.
- Bekar, L.K., He, W., and Nedergaard, M. (2008). Locus coeruleus alpha-adrenergic-mediated activation of cortical astrocytes in vivo. *Cereb. Cortex* *18*, 2789–2795.
- Bender, C.L., Sun, X., Farooq, M., Yang, Q., Davison, C., Maroteaux, M., Huang, Y.-S., Ishikawa, Y., and Liu, S.J. (2020). Emotional Stress Induces Structural Plasticity in Bergmann Glial Cells via an AC5-CPEB3-GluA1 Pathway. *J. Neurosci.* *40*, 3374–3384.
- Berger, B., Tassin, J.P., Blanc, G., Moyne, M.A., and Thierry, A.M. (1974). Histochemical confirmation for dopaminergic innervation of the rat cerebral cortex after destruction of the noradrenergic ascending pathways. *Brain Res.* *81*, 332–337.
- Berridge, C.W., Devilbiss, D.M., Andrzejewski, M.E., Arnsten, A.F.T., Kelley, A.E., Schmeichel, B., Hamilton, C., and Spencer, R.C. (2006). Methylphenidate preferentially increases catecholamine neurotransmission within the prefrontal cortex at low doses that enhance cognitive function. *Biol. Psychiatry* *60*, 1111–1120.
- Bezzi, P., Gundersen, V., Galbete, J.L., Seifert, G., Steinhäuser, C., Pilati, E., and Volterra, A. (2004). Astrocytes contain a vesicular compartment that is competent for regulated exocytosis of glutamate. *Nat. Neurosci.* *7*, 613–620.
- Bonaventura, J., Rico, A.J., Moreno, E., Sierra, S., Sánchez, M., Luquin, N., Farré, D., Müller, C.E., Martínez-Pinilla, E., Cortés, A., et al. (2014). L-DOPA-treatment in primates disrupts the expression of A(2A) adenosine-CB(1) cannabinoid-D(2) dopamine receptor heteromers in the caudate nucleus. *Neuropharmacology* *79*, 90–100.
- Brozowski, T.J., Brown, R.M., Rosvold, H.E., and Goldman, P.S. (1979). Cognitive deficit caused by regional depletion of dopamine in prefrontal cortex of rhesus monkey. *Science* *205*, 929–932.
- Bushong, E.A., Martone, M.E., Jones, Y.Z., and Ellisman, M.H. (2002). Protoplasmic astrocytes in CA1 stratum radiatum occupy separate anatomical domains. *J. Neurosci.* *22*, 183–192.
- Calebiro, D., Nikolaev, V.O., Gagliani, M.C., de Filippis, T., Dees, C., Tacchetti, C., Persani, L., and Lohse, M.J. (2009). Persistent cAMP-signals triggered by internalized G-protein-coupled receptors. *PLoS Biol.* *7*, e1000172.
- Cao, X., Li, L.-P., Wang, Q., Wu, Q., Hu, H.-H., Zhang, M., Fang, Y.-Y., Zhang, J., Li, S.-J., Xiong, W.-C., et al. (2013). Astrocyte-derived ATP modulates depressive-like behaviors. *Nat. Med.* *19*, 773–777.
- Cavanagh, S.E., Towers, J.P., Wallis, J.D., Hunt, L.T., and Kennerley, S.W. (2018). Reconciling persistent and dynamic hypotheses of working memory coding in prefrontal cortex. *Nat. Commun.* *9*,

3498.

- Chai, H., Diaz-Castro, B., Shigetomi, E., Monte, E., Oceau, J.C., Yu, X., Cohn, W., Rajendran, P.S., Vondriska, T.M., Whitelegge, J.P., et al. (2017). Neural Circuit-Specialized Astrocytes: Transcriptomic, Proteomic, Morphological, and Functional Evidence. *Neuron* 95, 531–549.e9.
- Chen, L., Bohanick, J.D., Nishihara, M., Seamans, J.K., and Yang, C.R. (2007). Dopamine D1/5 receptor-mediated long-term potentiation of intrinsic excitability in rat prefrontal cortical neurons: Ca<sup>2+</sup>-dependent intracellular signaling. *J. Neurophysiol.* 97, 2448–2464.
- Cilz, N.I., Kurada, L., Hu, B., and Lei, S. (2014). Dopaminergic modulation of GABAergic transmission in the entorhinal cortex: concerted roles of  $\alpha 1$  adrenoreceptors, inward rectifier K<sup>+</sup>, and T-type Ca<sup>2+</sup> channels. *Cereb. Cortex* 24, 3195–3208.
- Constantinidis, C., Funahashi, S., Lee, D., Murray, J.D., Qi, X.-L., Wang, M., and Arnsten, A.F.T. (2018). Persistent spiking activity underlies working memory. *J. Neurosci.* 38, 7020–7028.
- Corkrum, M., Covelo, A., Lines, J., Bellocchio, L., Pisansky, M., Loke, K., Quintana, R., Rothwell, P.E., Lujan, R., Marsicano, G., et al. (2020). Dopamine-Evoked Synaptic Regulation in the Nucleus Accumbens Requires Astrocyte Activity. *Neuron* 105, 1036–1047.e5.
- Cornil, C.A., and Ball, G.F. (2008). Interplay among catecholamine systems: dopamine binds to alpha2-adrenergic receptors in birds and mammals. *J. Comp. Neurol.* 511, 610–627.
- Cornil, C.A., Balthazart, J., Motte, P., Massotte, L., and Seutin, V. (2002). Dopamine activates noradrenergic receptors in the preoptic area. *J. Neurosci.* 22, 9320–9330.
- Courtney, N.A., and Ford, C.P. (2014). The timing of dopamine- and noradrenaline-mediated transmission reflects underlying differences in the extent of spillover and pooling. *J. Neurosci.* 34, 7645–7656.
- Cui, M., Aras, R., Christian, W.V., Rappold, P.M., Hatwar, M., Panza, J., Jackson-Lewis, V., Javitch, J.A., Ballatori, N., Przedborski, S., et al. (2009). The organic cation transporter-3 is a pivotal modulator of neurodegeneration in the nigrostriatal dopaminergic pathway. *Proc. Natl. Acad. Sci. USA* 106, 8043–8048.
- Cui, Q., Pitt, J.E., Pamukcu, A., Poulin, J.-F., Mabrouk, O.S., Fiske, M.P., Fan, I.B., Augustine, E.C., Young, K.A., Kennedy, R.T., et al. (2016). Blunted mGluR Activation Disinhibits Striatopallidal Transmission in Parkinsonian Mice. *Cell Rep.* 17, 2431–2444.
- D’Ascenzo, M., Fellin, T., Terunuma, M., Revilla-Sanchez, R., Meaney, D.F., Auberson, Y.P., Moss, S.J., and Haydon, P.G. (2007). mGluR5 stimulates gliotransmission in the nucleus accumbens. *Proc. Natl. Acad. Sci. USA* 104, 1995–2000.
- Devoto, P., Flore, G., Saba, P., Fà, M., and Gessa, G.L. (2005). Co-release of noradrenaline and dopamine in the cerebral cortex elicited by single train and repeated train stimulation of the locus

- coeruleus. *BMC Neurosci.* *6*, 31.
- Dias, R., Robbins, T.W., and Roberts, A.C. (1996). Primate analogue of the Wisconsin Card Sorting Test: effects of excitotoxic lesions of the prefrontal cortex in the marmoset. *Behav. Neurosci.* *110*, 872–886.
- Ding, F., O'Donnell, J., Thrane, A.S., Zeppenfeld, D., Kang, H., Xie, L., Wang, F., and Nedergaard, M. (2013).  $\alpha$ 1-Adrenergic receptors mediate coordinated Ca<sup>2+</sup> signaling of cortical astrocytes in awake, behaving mice. *Cell Calcium* *54*, 387–394.
- Dos Santos Pereira, J.N., Tadjerpisheh, S., Abu Abed, M., Saadatmand, A.R., Weksler, B., Romero, I.A., Couraud, P.-O., Brockmüller, J., and Tzvetkov, M.V. (2014). The poorly membrane permeable antipsychotic drugs amisulpride and sulpiride are substrates of the organic cation transporters from the SLC22 family. *AAPS J.* *16*, 1247–1258.
- Duan, H., and Wang, J. (2010). Selective transport of monoamine neurotransmitters by human plasma membrane monoamine transporter and organic cation transporter 3. *J. Pharmacol. Exp. Ther.* *335*, 743–753.
- Dubbs, A., Guevara, J., and Yuste, R. (2016). moco: Fast Motion Correction for Calcium Imaging. *Front Neuroinformatics* *10*, 6.
- Edelmann, E., and Lessmann, V. (2018). Dopaminergic innervation and modulation of hippocampal networks. *Cell Tissue Res.* *373*, 711–727.
- Feng, J., Zhang, C., Lischinsky, J.E., Jing, M., Zhou, J., Wang, H., Zhang, Y., Dong, A., Wu, Z., Wu, H., et al. (2019). A genetically encoded fluorescent sensor for rapid and specific in vivo detection of norepinephrine. *Neuron* *102*, 745–761.e8.
- Fischer, T., Scheffler, P., and Lohr, C. (2020). Dopamine-induced calcium signaling in olfactory bulb astrocytes. *Sci. Rep.* *10*, 631.
- Frederick, A.L., Yano, H., Trifilieff, P., Vishwasrao, H.D., Biezonski, D., Mészáros, J., Urizar, E., Sibley, D.R., Kellendonk, C., Sonntag, K.C., et al. (2015). Evidence against dopamine D1/D2 receptor heteromers. *Mol. Psychiatry* *20*, 1373–1385.
- Fritschy, J.M., and Grzanna, R. (1989). Immunohistochemical analysis of the neurotoxic effects of DSP-4 identifies two populations of noradrenergic axon terminals. *Neuroscience* *30*, 181–197.
- Funahashi, S., Bruce, C.J., and Goldman-Rakic, P.S. (1989). Mnemonic coding of visual space in the monkey's dorsolateral prefrontal cortex. *J. Neurophysiol.* *61*, 331–349.
- Fuster, J.M., and Alexander, G.E. (1971). Neuron activity related to short-term memory. *Science* *173*, 652–654.
- Fuster, J.M., Bodner, M., and Kroger, J.K. (2000). Cross-modal and cross-temporal association in neurons of frontal cortex. *Nature* *405*, 347–351.

- Gao, W.-J., and Goldman-Rakic, P.S. (2003). Selective modulation of excitatory and inhibitory microcircuits by dopamine. *Proc. Natl. Acad. Sci. USA* *100*, 2836–2841.
- Gao, W.-J., Wang, Y., and Goldman-Rakic, P.S. (2003). Dopamine modulation of perisomatic and peridendritic inhibition in prefrontal cortex. *J. Neurosci.* *23*, 1622–1630.
- Garris, P.A., and Wightman, R.M. (1994). Different kinetics govern dopaminergic transmission in the amygdala, prefrontal cortex, and striatum: an in vivo voltammetric study. *J. Neurosci.* *14*, 442–450.
- George, M.S., Ketter, T.A., Parekh, P.I., Horwitz, B., Herscovitch, P., and Post, R.M. (1995). Brain activity during transient sadness and happiness in healthy women. *Am. J. Psychiatry* *152*, 341–351.
- Goldman-Rakic, P.S. (1995). Cellular basis of working memory. *Neuron* *14*, 477–485.
- Gong, S., Zheng, C., Dougherty, M.L., Losos, K., Didkovsky, N., Schambra, U.B., Nowak, N.J., Joyner, A., Leblanc, G., Hatten, M.E., et al. (2003). A gene expression atlas of the central nervous system based on bacterial artificial chromosomes. *Nature* *425*, 917–925.
- González, S., Moreno-Delgado, D., Moreno, E., Pérez-Capote, K., Franco, R., Mallol, J., Cortés, A., Casadó, V., Lluís, C., Ortiz, J., et al. (2012). Circadian-related heteromerization of adrenergic and dopamine D<sub>4</sub> receptors modulates melatonin synthesis and release in the pineal gland. *PLoS Biol.* *10*, e1001347.
- Gordon, G.R.J., Baimoukhametova, D.V., Hewitt, S.A., Rajapaksha, W.R.A.K.J.S., Fisher, T.E., and Bains, J.S. (2005). Norepinephrine triggers release of glial ATP to increase postsynaptic efficacy. *Nat. Neurosci.* *8*, 1078–1086.
- Gresch, P.J., Sved, A.F., Zigmond, M.J., and Finlay, J.M. (1994). Stress-induced sensitization of dopamine and norepinephrine efflux in medial prefrontal cortex of the rat. *J. Neurochem.* *63*, 575–583.
- Guiard, B.P., El Mansari, M., and Blier, P. (2008). Cross-talk between dopaminergic and noradrenergic systems in the rat ventral tegmental area, locus ceruleus, and dorsal hippocampus. *Mol. Pharmacol.* *74*, 1463–1475.
- Harada, K., Ito, M., Wang, X., Tanaka, M., Wongso, D., Konno, A., Hirai, H., Hirase, H., Tsuboi, T., and Kitaguchi, T. (2017). Red fluorescent protein-based cAMP indicator applicable to optogenetics and in vivo imaging. *Sci. Rep.* *7*, 7351.
- Hariri, A.R., Mattay, V.S., Tessitore, A., Fera, F., and Weinberger, D.R. (2003). Neocortical modulation of the amygdala response to fearful stimuli. *Biol. Psychiatry* *53*, 494–501.
- Huang, Y.-Y., Simpson, E., Kellendonk, C., and Kandel, E.R. (2004). Genetic evidence for the bidirectional modulation of synaptic plasticity in the prefrontal cortex by D1 receptors. *Proc. Natl. Acad. Sci. USA* *101*, 3236–3241.
- Hurst, J.L., and West, R.S. (2010). Taming anxiety in laboratory mice. *Nat. Methods* *7*, 825–826.

- Inagaki, H.K., Fontolan, L., Romani, S., and Svoboda, K. (2019). Discrete attractor dynamics underlies persistent activity in the frontal cortex. *Nature* 566, 212–217.
- Irannejad, R., Tomshine, J.C., Tomshine, J.R., Chevalier, M., Mahoney, J.P., Steyaert, J., Rasmussen, S.G.F., Sunahara, R.K., El-Samad, H., Huang, B., et al. (2013). Conformational biosensors reveal GPCR signalling from endosomes. *Nature* 495, 534–538.
- Jennings, A., Tyurikova, O., Bard, L., Zheng, K., Semyanov, A., Henneberger, C., and Rusakov, D.A. (2017). Dopamine elevates and lowers astroglial Ca<sup>2+</sup> through distinct pathways depending on local synaptic circuitry. *Glia* 65, 447–459.
- John, C.S., Smith, K.L., Van't Veer, A., Gompf, H.S., Carlezon, W.A., Cohen, B.M., Öngür, D., and Bechtholt-Gompf, A.J. (2012). Blockade of astrocytic glutamate uptake in the prefrontal cortex induces anhedonia. *Neuropsychopharmacology* 37, 2467–2475.
- Kamigaki, T., and Dan, Y. (2017). Delay activity of specific prefrontal interneuron subtypes modulates memory-guided behavior. *Nat. Neurosci.* 20, 854–863.
- Kempadoo, K.A., Mosharov, E.V., Choi, S.J., Sulzer, D., and Kandel, E.R. (2016). Dopamine release from the locus coeruleus to the dorsal hippocampus promotes spatial learning and memory. *Proc. Natl. Acad. Sci. USA* 113, 14835–14840.
- Kesner, R.P., Hunt, M.E., Williams, J.M., and Long, J.M. (1996). Prefrontal cortex and working memory for spatial response, spatial location, and visual object information in the rat. *Cereb. Cortex* 6, 311–318.
- Khakh, B.S., and Sofroniew, M.V. (2015). Diversity of astrocyte functions and phenotypes in neural circuits. *Nat. Neurosci.* 18, 942–952.
- Kim, D., Jeong, H., Lee, J., Ghim, J.-W., Her, E.S., Lee, S.-H., and Jung, M.W. (2016). Distinct Roles of Parvalbumin- and Somatostatin-Expressing Interneurons in Working Memory. *Neuron* 92, 902–915.
- Kim, H., Somerville, L.H., Johnstone, T., Alexander, A.L., and Whalen, P.J. (2003). Inverse amygdala and medial prefrontal cortex responses to surprised faces. *Neuroreport* 14, 2317–2322.
- Kirshner, N. (1957). Pathway of noradrenaline formation from DOPA. *J. Biol. Chem.* 226, 821–825.
- Kofuji, P., and Araque, A. (2021). G-Protein-Coupled Receptors in Astrocyte-Neuron Communication. *Neuroscience* 456, 71–84.
- Kol, A., Adamsky, A., Groysman, M., Kreisel, T., London, M., and Goshen, I. (2020). Astrocytes contribute to remote memory formation by modulating hippocampal-cortical communication during learning. *Nat. Neurosci.* 23, 1229–1239.
- Kolasa, M., Solich, J., Faron-Górecka, A., Żurawek, D., Pabian, P., Łukasiewicz, S., Kuśmider, M., Szafran-Pilch, K., Szlachta, M., and Dziedzicka-Wasylewska, M. (2018). Paroxetine and Low-dose Risperidone Induce Serotonin 5-HT<sub>1A</sub> and Dopamine D<sub>2</sub> Receptor Heteromerization in the Mouse

- Prefrontal Cortex. *Neuroscience* 377, 184–196.
- Kotowski, S.J., Hopf, F.W., Seif, T., Bonci, A., and von Zastrow, M. (2011). Endocytosis promotes rapid dopaminergic signaling. *Neuron* 71, 278–290.
- Kröner, S., Krimer, L.S., Lewis, D.A., and Barrionuevo, G. (2007). Dopamine increases inhibition in the monkey dorsolateral prefrontal cortex through cell type-specific modulation of interneurons. *Cereb. Cortex* 17, 1020–1032.
- Lalo, U., Palygin, O., Rasooli-Nejad, S., Andrew, J., Haydon, P.G., and Pankratov, Y. (2014). Exocytosis of ATP from astrocytes modulates phasic and tonic inhibition in the neocortex. *PLoS Biol.* 12, e1001747.
- Lammel, S., Hetzel, A., Häckel, O., Jones, I., Liss, B., and Roeper, J. (2008). Unique properties of mesoprefrontal neurons within a dual mesocorticolimbic dopamine system. *Neuron* 57, 760–773.
- Lammel, S., Lim, B.K., Ran, C., Huang, K.W., Betley, M.J., Tye, K.M., Deisseroth, K., and Malenka, R.C. (2012). Input-specific control of reward and aversion in the ventral tegmental area. *Nature* 491, 212–217.
- Lanjakornsiripan, D., Pior, B.-J., Kawaguchi, D., Furutachi, S., Tahara, T., Katsuyama, Y., Suzuki, Y., Fukazawa, Y., and Gotoh, Y. (2018). Layer-specific morphological and molecular differences in neocortical astrocytes and their dependence on neuronal layers. *Nat. Commun.* 9, 1623.
- Lee, S.J., Lodder, B., Chen, Y., Patriarchi, T., Tian, L., and Sabatini, B.L. (2021). Cell-type-specific asynchronous modulation of PKA by dopamine in learning. *Nature* 590, 451–456.
- Lee, S.P., So, C.H., Rashid, A.J., Varghese, G., Cheng, R., Lança, A.J., O’Dowd, B.F., and George, S.R. (2004). Dopamine D1 and D2 receptor Co-activation generates a novel phospholipase C-mediated calcium signal. *J. Biol. Chem.* 279, 35671–35678.
- Lee, Y., Son, H., Kim, G., Kim, S., Lee, D.H., Roh, G.S., Kang, S.S., Cho, G.J., Choi, W.S., and Kim, H.J. (2013). Glutamine deficiency in the prefrontal cortex increases depressive-like behaviours in male mice. *J. Psychiatry Neurosci.* 38, 183–191.
- Levene, M.J., Dombeck, D.A., Kasischke, K.A., Molloy, R.P., and Webb, W.W. (2004). In vivo multiphoton microscopy of deep brain tissue. *J. Neurophysiol.* 91, 1908–1912.
- Li, X., Zima, A.V., Sheikh, F., Blatter, L.A., and Chen, J. (2005). Endothelin-1-induced arrhythmogenic Ca<sup>2+</sup> signaling is abolished in atrial myocytes of inositol-1,4,5-trisphosphate(IP3)-receptor type 2-deficient mice. *Circ. Res.* 96, 1274–1281.
- Lima, A., Sardinha, V.M., Oliveira, A.F., Reis, M., Mota, C., Silva, M.A., Marques, F., Cerqueira, J.J., Pinto, L., Sousa, N., et al. (2014). Astrocyte pathology in the prefrontal cortex impairs the cognitive function of rats. *Mol. Psychiatry* 19, 834–841.
- Lohani, S., Martig, A.K., Deisseroth, K., Witten, I.B., and Moghaddam, B. (2019). Dopamine modulation

- of prefrontal cortex activity is manifold and operates at multiple temporal and spatial scales. *Cell Rep.* 27, 99–114.e6.
- Marek, G.J., and Aghajanian, G.K. (1999). 5-HT<sub>2A</sub> receptor or  $\alpha$ 1-adrenoceptor activation induces excitatory postsynaptic currents in layer V pyramidal cells of the medial prefrontal cortex. *Eur. J. Pharmacol.* 367, 197–206.
- Martín, R., Bajo-Grañeras, R., Moratalla, R., Perea, G., and Araque, A. (2015). Circuit-specific signaling in astrocyte-neuron networks in basal ganglia pathways. *Science* 349, 730–734.
- Martin-Fernandez, M., Jamison, S., Robin, L.M., Zhao, Z., Martin, E.D., Aguilar, J., Benneyworth, M.A., Marsicano, G., and Araque, A. (2017). Synapse-specific astrocyte gating of amygdala-related behavior. *Nat. Neurosci.* 20, 1540–1548.
- Matsuda, Y., Marzo, A., and Otani, S. (2006). The presence of background dopamine signal converts long-term synaptic depression to potentiation in rat prefrontal cortex. *J. Neurosci.* 26, 4803–4810.
- Mederos, S., Sánchez-Puelles, C., Esparza, J., Valero, M., Ponomarenko, A., and Perea, G. (2021). GABAergic signaling to astrocytes in the prefrontal cortex sustains goal-directed behaviors. *Nat. Neurosci.* 24, 82–92.
- Medvedev, I.O., Ramsey, A.J., Masoud, S.T., Bermejo, M.K., Urs, N., Sotnikova, T.D., Beaulieu, J.-M., Gainetdinov, R.R., and Salahpour, A. (2013). D1 dopamine receptor coupling to PLC $\beta$  regulates forward locomotion in mice. *J. Neurosci.* 33, 18125–18133.
- Milad, M.R., and Quirk, G.J. (2002). Neurons in medial prefrontal cortex signal memory for fear extinction. *Nature* 420, 70–74.
- Mitrano, D.A., Pare, J.F., Smith, Y., and Weinshenker, D. (2014). D1-dopamine and  $\alpha$ 1-adrenergic receptors co-localize in dendrites of the rat prefrontal cortex. *Neuroscience* 258, 90–100.
- Moreno, E., Moreno-Delgado, D., Navarro, G., Hoffmann, H.M., Fuentes, S., Rosell-Vilar, S., Gasperini, P., Rodríguez-Ruiz, M., Medrano, M., Mallol, J., et al. (2014). Cocaine disrupts histamine H3 receptor modulation of dopamine D1 receptor signaling:  $\sigma$ 1-D1-H3 receptor complexes as key targets for reducing cocaine's effects. *J. Neurosci.* 34, 3545–3558.
- Morón, J.A., Brockington, A., Wise, R.A., Rocha, B.A., and Hope, B.T. (2002). Dopamine uptake through the norepinephrine transporter in brain regions with low levels of the dopamine transporter: evidence from knock-out mouse lines. *J. Neurosci.* 22, 389–395.
- Muller, A., Joseph, V., Slesinger, P.A., and Kleinfeld, D. (2014). Cell-based reporters reveal in vivo dynamics of dopamine and norepinephrine release in murine cortex. *Nat. Methods* 11, 1245–1252.
- Muntean, B.S., Zucca, S., MacMullen, C.M., Dao, M.T., Johnston, C., Iwamoto, H., Blakely, R.D., Davis, R.L., and Martemyanov, K.A. (2018). Interrogating the Spatiotemporal Landscape of Neuromodulatory GPCR Signaling by Real-Time Imaging of cAMP in Intact Neurons and Circuits.

Cell Rep. 22, 255–268.

- Murphy-Royal, C., Johnston, A.D., Boyce, A.K.J., Diaz-Castro, B., Institoris, A., Peringod, G., Zhang, O., Stout, R.F., Spray, D.C., Thompson, R.J., et al. (2020). Stress gates an astrocytic energy reservoir to impair synaptic plasticity. *Nat. Commun.* 11, 2014.
- Nagai, J., Rajbhandari, A.K., Gangwani, M.R., Hachisuka, A., Coppola, G., Masmanidis, S.C., Fanselow, M.S., and Khakh, B.S. (2019). Hyperactivity with Disrupted Attention by Activation of an Astrocyte Synaptogenic Cue. *Cell* 177, 1280–1292.e20.
- Navarro, G., Cordoní, A., Casadó-Anguera, V., Moreno, E., Cai, N.-S., Cortés, A., Canela, E.I., Dessauer, C.W., Casadó, V., Pardo, L., et al. (2018). Evidence for functional pre-coupled complexes of receptor heteromers and adenylyl cyclase. *Nat. Commun.* 9, 1242.
- Nicola, S.M., and Malenka, R.C. (1997). Dopamine depresses excitatory and inhibitory synaptic transmission by distinct mechanisms in the nucleus accumbens. *J. Neurosci.* 17, 5697–5710.
- Nomura, S., Bouhadana, M., Morel, C., Faure, P., Cauli, B., Lambolez, B., and Hepp, R. (2014). Noradrenalin and dopamine receptors both control cAMP-PKA signaling throughout the cerebral cortex. *Front. Cell Neurosci.* 8, 247.
- Oe, Y., Wang, X., Patriarchi, T., Konno, A., Ozawa, K., Yahagi, K., Hirai, H., Tsuboi, T., Kitaguchi, T., Tian, L., et al. (2020). Distinct temporal integration of noradrenaline signaling by astrocytic second messengers during vigilance. *Nat. Commun.* 11, 471.
- Özkan, M., Johnson, N.W., Sehirli, U.S., Woodhall, G.L., and Stanford, I.M. (2017). Dopamine acting at D1-like, D2-like and  $\alpha$ 1-adrenergic receptors differentially modulates theta and gamma oscillatory activity in primary motor cortex. *PLoS One* 12, e0181633.
- Panatier, A., Vallée, J., Haber, M., Murai, K.K., Lacaille, J.-C., and Robitaille, R. (2011). Astrocytes are endogenous regulators of basal transmission at central synapses. *Cell* 146, 785–798.
- Pankratov, Y., and Lalo, U. (2015). Role for astroglial  $\alpha$ 1-adrenoreceptors in gliotransmission and control of synaptic plasticity in the neocortex. *Front. Cell Neurosci.* 9, 230.
- Park, J.C., Bae, J.W., Kim, J., and Jung, M.W. (2019). Dynamically changing neuronal activity supporting working memory for predictable and unpredictable durations. *Sci. Rep.* 9, 15512.
- Pascual, O., Casper, K.B., Kubera, C., Zhang, J., Revilla-Sanchez, R., Sul, J.-Y., Takano, H., Moss, S.J., McCarthy, K., and Haydon, P.G. (2005). Astrocytic purinergic signaling coordinates synaptic networks. *Science* 310, 113–116.
- Patriarchi, T., Cho, J.R., Merten, K., Howe, M.W., Marley, A., Xiong, W.-H., Folk, R.W., Broussard, G.J., Liang, R., Jang, M.J., et al. (2018). Ultrafast neuronal imaging of dopamine dynamics with designed genetically encoded sensors. *Science* 360.
- Patriarchi, T., Mohebi, A., Sun, J., Marley, A., Liang, R., Dong, C., Puhger, K., Mizuno, G.O., Davis,

- C.M., Wiltgen, B., et al. (2020). An expanded palette of dopamine sensors for multiplex imaging in vivo. *Nat. Methods* *17*, 1147–1155.
- Paukert, M., Agarwal, A., Cha, J., Doze, V.A., Kang, J.U., and Bergles, D.E. (2014). Norepinephrine controls astroglial responsiveness to local circuit activity. *Neuron* *82*, 1263–1270.
- Pelassa, S., Guidolin, D., Venturini, A., Averna, M., Frumento, G., Campanini, L., Bernardi, R., Cortelli, P., Buonaura, G.C., Maura, G., et al. (2019). A2A-D2 Heteromers on Striatal Astrocytes: Biochemical and Biophysical Evidence. *Int. J. Mol. Sci.* *20*.
- Perea, G., and Araque, A. (2007). Astrocytes potentiate transmitter release at single hippocampal synapses. *Science* *317*, 1083–1086.
- Petravicz, J., Fiacco, T.A., and McCarthy, K.D. (2008). Loss of IP3 receptor-dependent Ca<sup>2+</sup> increases in hippocampal astrocytes does not affect baseline CA1 pyramidal neuron synaptic activity. *J. Neurosci.* *28*, 4967–4973.
- Petrelli, F., Dallérac, G., Pucci, L., Cali, C., Zehnder, T., Sultan, S., Lecca, S., Chicca, A., Ivanov, A., Asensio, C.S., et al. (2020). Dysfunction of homeostatic control of dopamine by astrocytes in the developing prefrontal cortex leads to cognitive impairments. *Mol. Psychiatry* *25*, 732–749.
- Pinto, L., and Dan, Y. (2015). Cell-Type-Specific Activity in Prefrontal Cortex during Goal-Directed Behavior. *Neuron* *87*, 437–450.
- Porter, J.T., and McCarthy, K.D. (1997). Astrocytic neurotransmitter receptors in situ and in vivo. *Prog. Neurobiol.* *51*, 439–455.
- Poskanzer, K.E., and Yuste, R. (2016). Astrocytes regulate cortical state switching in vivo. *Proc. Natl. Acad. Sci. USA* *113*, E2675–84.
- Pougnnet, J.-T., Toulme, E., Martinez, A., Choquet, D., Hosy, E., and Boué-Grabot, E. (2014). ATP P2X receptors downregulate AMPA receptor trafficking and postsynaptic efficacy in hippocampal neurons. *Neuron* *83*, 417–430.
- Proudman, R.G.W., and Baker, J.G. (2021). The selectivity of  $\alpha$ -adrenoceptor agonists for the human  $\alpha$ 1A,  $\alpha$ 1B, and  $\alpha$ 1D-adrenoceptors. *Pharmacol. Res. Perspect.* *9*, e00799.
- Ragozzino, M.E., Detrick, S., and Kesner, R.P. (1999). Involvement of the prelimbic-infralimbic areas of the rodent prefrontal cortex in behavioral flexibility for place and response learning. *J. Neurosci.* *19*, 4585–4594.
- Rebois, R.V., Maki, K., Meeks, J.A., Fishman, P.H., Hébert, T.E., and Northup, J.K. (2012). D2-like dopamine and  $\beta$ -adrenergic receptors form a signaling complex that integrates Gs- and Gi-mediated regulation of adenylyl cyclase. *Cell Signal.* *24*, 2051–2060.
- Rosenkranz, J.A., and Grace, A.A. (2001). Dopamine attenuates prefrontal cortical suppression of sensory inputs to the basolateral amygdala of rats. *J. Neurosci.* *21*, 4090–4103.

- Sahu, A., Tyeryar, K.R., Vongtau, H.O., Sibley, D.R., and Undieh, A.S. (2009). D5 dopamine receptors are required for dopaminergic activation of phospholipase C. *Mol. Pharmacol.* 75, 447–453.
- Sardinha, V.M., Guerra-Gomes, S., Caetano, I., Tavares, G., Martins, M., Reis, J.S., Correia, J.S., Teixeira-Castro, A., Pinto, L., Sousa, N., et al. (2017). Astrocytic signaling supports hippocampal-prefrontal theta synchronization and cognitive function. *Glia* 65, 1944–1960.
- Seamans, J.K., Gorelova, N., Durstewitz, D., and Yang, C.R. (2001). Bidirectional dopamine modulation of GABAergic inhibition in prefrontal cortical pyramidal neurons. *J. Neurosci.* 21, 3628–3638.
- Sesack, S.R., Hawrylak, V.A., Matus, C., Guido, M.A., and Levey, A.I. (1998). Dopamine axon varicosities in the prelimbic division of the rat prefrontal cortex exhibit sparse immunoreactivity for the dopamine transporter. *J. Neurosci.* 18, 2697–2708.
- Shigetomi, E., Kracun, S., Sofroniew, M.V., and Khakh, B.S. (2010). A genetically targeted optical sensor to monitor calcium signals in astrocyte processes. *Nat. Neurosci.* 13, 759–766.
- Shuen, J.A., Chen, M., Gloss, B., and Calakos, N. (2008). *Drd1a*-tdTomato BAC transgenic mice for simultaneous visualization of medium spiny neurons in the direct and indirect pathways of the basal ganglia. *J. Neurosci.* 28, 2681–2685.
- Simard, S., Coppola, G., Rudyk, C.A., Hayley, S., McQuaid, R.J., and Salmaso, N. (2018). Profiling changes in cortical astroglial cells following chronic stress. *Neuropsychopharmacology* 43, 1961–1971.
- Slezak, M., Kandler, S., Van Veldhoven, P.P., Van den Haute, C., Bonin, V., and Holt, M.G. (2019). Distinct Mechanisms for Visual and Motor-Related Astrocyte Responses in Mouse Visual Cortex. *Curr. Biol.* 29, 3120–3127.e5.
- Smith, C.C., and Greene, R.W. (2012). CNS dopamine transmission mediated by noradrenergic innervation. *J. Neurosci.* 32, 6072–6080.
- Spaak, E., Watanabe, K., Funahashi, S., and Stokes, M.G. (2017). Stable and dynamic coding for working memory in primate prefrontal cortex. *J. Neurosci.* 37, 6503–6516.
- Srinivasan, R., Lu, T.-Y., Chai, H., Xu, J., Huang, B.S., Golshani, P., Coppola, G., and Khakh, B.S. (2016). New transgenic mouse lines for selectively targeting astrocytes and studying calcium signals in astrocyte processes in situ and in vivo. *Neuron* 92, 1181–1195.
- Stanford, S.C., and Heal, D.J. (2019). Catecholamines: Knowledge and understanding in the 1960s, now, and in the future. *Brain Neurosci. Adv.* 3, 2398212818810682.
- Steinberg, S.F., and Bilezikian, J.P. (1982). Identification and characterization of alpha 1 adrenergic receptors in rat myocardium with a new iodinated radioligand, [125I]IBE 2254. *J. Mol. Cell Cardiol.* 14, 601–610.
- Sun, F., Zeng, J., Jing, M., Zhou, J., Feng, J., Owen, S.F., Luo, Y., Li, F., Wang, H., Yamaguchi, T., et al.

- (2018). A genetically encoded fluorescent sensor enables rapid and specific detection of dopamine in flies, fish, and mice. *Cell* 174, 481–496.e19.
- Takeuchi, T., Duzskiewicz, A.J., Sonneborn, A., Spooner, P.A., Yamasaki, M., Watanabe, M., Smith, C.C., Fernández, G., Deisseroth, K., Greene, R.W., et al. (2016). Locus coeruleus and dopaminergic consolidation of everyday memory. *Nature* 537, 357–362.
- Thierry, A.M., Tassin, J.P., Blanc, G., and Glowinski, J. (1976). Selective activation of mesocortical DA system by stress. *Nature* 263, 242–244.
- Trifilieff, P., Rives, M.-L., Urizar, E., Piskowski, R.A., Vishwasrao, H.D., Castrillon, J., Schmauss, C., Slättman, M., Gullberg, M., and Javitch, J.A. (2011). Detection of antigen interactions ex vivo by proximity ligation assay: endogenous dopamine D2-adenosine A2A receptor complexes in the striatum. *BioTechniques* 51, 111–118.
- Tsai, H.-H., Li, H., Fuentealba, L.C., Molofsky, A.V., Taveira-Marques, R., Zhuang, H., Tenney, A., Murnen, A.T., Fancy, S.P.J., Merkle, F., et al. (2012). Regional astrocyte allocation regulates CNS synaptogenesis and repair. *Science* 337, 358–362.
- Undie, A.S., and Friedman, E. (1990). Stimulation of a dopamine D1 receptor enhances inositol phosphates formation in rat brain. *J. Pharmacol. Exp. Ther.* 253, 987–992.
- Valle-León, M., Callado, L.F., Aso, E., Cajiao-Manrique, M.M., Sahlholm, K., López-Cano, M., Soler, C., Altafaj, X., Watanabe, M., Ferré, S., et al. (2021). Decreased striatal adenosine A2A-dopamine D2 receptor heteromerization in schizophrenia. *Neuropsychopharmacology* 46, 665–672.
- Vander Weele, C.M., Siciliano, C.A., Matthews, G.A., Namburi, P., Izadmehr, E.M., Espinel, I.C., Nieh, E.H., Schut, E.H.S., Padilla-Coreano, N., Burgos-Robles, A., et al. (2018). Dopamine enhances signal-to-noise ratio in cortical-brainstem encoding of aversive stimuli. *Nature* 563, 397–401.
- Vijayraghavan, S., Wang, M., Birnbaum, S.G., Williams, G.V., and Arnsten, A.F.T. (2007). Inverted-U dopamine D1 receptor actions on prefrontal neurons engaged in working memory. *Nat. Neurosci.* 10, 376–384.
- Wang, Q., Kong, Y., Wu, D.-Y., Liu, J.-H., Jie, W., You, Q.-L., Huang, L., Hu, J., Chu, H.-D., Gao, F., et al. (2021). Impaired calcium signaling in astrocytes modulates autism spectrum disorder-like behaviors in mice. *Nat. Commun.* 12, 3321.
- Wang, Y., DelRosso, N.V., Vaidyanathan, T.V., Cahill, M.K., Reitman, M.E., Pittolo, S., Mi, X., Yu, G., and Poskanzer, K.E. (2019). Accurate quantification of astrocyte and neurotransmitter fluorescence dynamics for single-cell and population-level physiology. *Nat. Neurosci.* 22, 1936–1944.
- Wu, Z., He, K., Chen, Y., Li, H., Pan, S., Li, B., Liu, T., Wang, H., Du, J., Jing, M., et al. (2021). An ultrasensitive GRAB sensor for detecting extracellular ATP in vitro and in vivo. *BioRxiv*.
- Xin, W., Schuebel, K.E., Jair, K.-W., Cimbri, R., De Biase, L.M., Goldman, D., and Bonci, A. (2019).

- Ventral midbrain astrocytes display unique physiological features and sensitivity to dopamine D2 receptor signaling. *Neuropsychopharmacology* *44*, 344–355.
- Yang, J., Vitery, M.D.C., Chen, J., Osei-Owusu, J., Chu, J., and Qiu, Z. (2019). Glutamate-Releasing SWELL1 Channel in Astrocytes Modulates Synaptic Transmission and Promotes Brain Damage in Stroke. *Neuron* *102*, 813–827.e6.
- Yapo, C., Nair, A.G., Clement, L., Castro, L.R., Hellgren Kotaleski, J., and Vincent, P. (2017). Detection of phasic dopamine by D1 and D2 striatal medium spiny neurons. *J. Physiol. (Lond.)* *595*, 7451–7475.
- Zhang, J., Wang, H., Ye, C., Ge, W., Chen, Y., Jiang, Z., Wu, C., Poo, M., and Duan, S. (2003). ATP released by astrocytes mediates glutamatergic activity-dependent heterosynaptic suppression. *Neuron* *40*, 971–982.
- Zhang, Y., Chen, K., Sloan, S.A., Bennett, M.L., Scholze, A.R., O’Keeffe, S., Phatnani, H.P., Guarnieri, P., Caneda, C., Ruderisch, N., et al. (2014). An RNA-sequencing transcriptome and splicing database of glia, neurons, and vascular cells of the cerebral cortex. *J. Neurosci.* *34*, 11929–11947.
- Zhu, Y., Dwork, A.J., Trifilieff, P., and Javitch, J.A. (2020). Detection of G Protein-Coupled Receptor Complexes in Postmortem Human Brain by Proximity Ligation Assay. *Curr Protoc Neurosci* *91*, e86.
- Zwart, R., Verhaagh, S., Buitelaar, M., Popp-Snijders, C., and Barlow, D.P. (2001). Impaired activity of the extraneuronal monoamine transporter system known as uptake-2 in *Orct3/Slc22a3*-deficient mice. *Mol. Cell. Biol.* *21*, 4188–4196.